Article:

Stockmeyer, J.M., Shaw, J.H., Brown, N.D. et al. (5 more authors) (2017) Active thrust sheet deformation over multiple rupture cycles: A quantitative basis for relating terrace folds to fault slip rates. Geological Society of America bulletin. ISSN 0016-7606

https://doi.org/10.1130/B31590.1

Active thrust sheet deformation over multiple rupture cycles: a quantitative basis for relating terrace folds to fault slip rates

Authors version of paper published at doi: 10.1130/B31590.1, GSA Bulletin B31590.1

Joseph M. Stockmeyer[1]*, John H. Shaw[1], Nathan D. Brown[2], Edward J. Rhodes[2,3], Paul W. Richardson[4], Maomao Wang[1], Leore C. Lavin[1], Shuwei Guan[5]

[1]Dept. of Earth & Planetary Sciences, Harvard University, 20 Oxford Street, Cambridge, MA, 02138, U.S.A.

[2]Dept. of Earth, Planetary, and Space Sciences, UCLA, 595 Charles Young Drive East, Box 951567, Los Angeles, CA 90095, U.S.A.

[3]Dept. of Geography, The University of Sheffield, Western Bank, Sheffield S10 2TN, U.K.

[4]Dept. of Geological Sciences, University of Oregon, 1272 University of Oregon, Eugene, OR 97403, U.S.A.

[5]Research Institute of Petroleum Exploration and Development (RIPED), PetroChina, 20 Xue Yuan Rd, Haidian District, Beijing, China, 100083

*Corresponding author (jstockmeyer@fas.harvard.edu)

ABSTRACT

Many recent thrust fault earthquakes have involved coseismic surface faulting and folding, revealing the multifaceted nature of active thrust sheet deformation. We integrate records of surface deformation, subsurface structure and geochronology to investigate active surface deformation over multiple rupture cycles across the Southern Junggar Thrust (SJT) in the southern Junggar basin, NW China. Fluvial terrace geometries – extracted from a 1-m digital elevation model – reveal records of surface faulting across a prominent fault scarp. In addition, terraces exhibit progressive folding across fold scarps. Fault and fold scarps are spatially coincident with a surface-emergent SJT splay and subsurface fault bends along the SJT, respectively, constrained by seismic reflection data. We quantify the magnitude of fault slip at depth implied by fold scarps along Holocene-aged terraces. Our method yields results consistent with independent estimates of slip implied by fault scarp relief for the same terraces. Four late Quaternary terrace records are less continuous, preserved only as fold scarps that suggest folding kinematics involving a component of limb rotation. We develop a new method for quantifying fault slip at depth from terrace folds using a mechanical forward modeling approach. Our analysis yields quantitative relations between fold dip and fault slip, allowing us to quantify SJT fault slip from terrace folds from ~250 ka-present. SJT fault slip rate has decelerated from ~7.0 mm/yr in the Late Quaternary to ~1.3 mm/yr throughout the Holocene. These results provide new insight into the kinematics of fault-bend folding for natural structures and define new methods to accurately estimate fault slip and slip rates from terrace folds in active thrust sheets.

INTRODUCTION

The destructive nature of convergent tectonics is manifest by large magnitude earthquakes that occur both along subduction zones and within fold-and-thrust belts. Contemporary events of this latter type (e.g., 1999 Mw 7.6 Chi-Chi, Taiwan; 2008 Mw 7.9 Wenchuan, China; 2015 M_w 7.8 Gorkha, Nepal) have led to tens of thousands of deaths and billions of dollars of damage to infrastructure. These earthquakes have also demonstrated some of the ongoing challenges associated with assessing the hazards posed by active thrust faults. Specifically, surface deformation associated with thrust fault earthquakes is multifaceted, often involving components of coseismic folding as well as surface faulting (e.g., Chen et al., 2007). Many active thrust faults - or portions of these faults – are blind, such that surface deformation is characterized exclusively by folding (e.g., Stein and King, 1984; Shaw and Suppe, 1994; Dolan et al., 2003). However, traditional, geologic methods of inferring fault activity, slip rate, and paleoearthquake magnitudes are based exclusively on characterizations of surface faulting deformation (e.g. Wells and Coppersmith, 1994; Wesnousky, 2006; 2008; Leonard, 2010). These methods prove inadequate, in cases where all or a portion of subsurface fault slip is manifest by folding at the surface. Thus, recent studies have made progress in adapting traditional paleoseismic methods to recover more accurate records of fault activity on blind thrust faults (e.g., Mueller et al., 1999; Pratt et al., 2002; Shaw et al., 2002; Dolan et al., 2003; Leon et al., 2007; 2009). These methods generally require kinematic fault-related folding models in order to quantitatively relate surface folding strains to fault activity.

Despite the challenges of constraining deformation in active thrust sheets, coupled faulting and folding deformation accumulated over geologic timescales has been recognized for decades (e.g., Rich, 1934; Dahlstrom, 1970) and their direct relationships are now well-established by fault-related folding theories (e.g. Suppe, 1993; Suppe and Medwedeff, 1990; Hardy and Poblet, 1995; Suppe et al., 2004; Shaw et al., 2005). The fundamental basis for these theories underscores the oft-observed occurrence of folds with faults: folding is driven by slip across fault-bends, at propagating fault tips, and along detachments – reflecting displacement gradients within a thrust sheet (Figure 1). This fault-related folding concept is central to our understanding of how shortening is accommodated in Earth's brittle crust over geologic time scales. Moreover, it has critical implications for seismic hazards assessment as it describes a range of ways that folding may reflect fault slip at depth. For example, a classic fault-bend fold (Suppe, 1983) predicts that fault slip remains constant as it is transmitted up a planar thrust ramp (Figure 1A). Thus, a measure of surface slip (SS) along an emergent thrust ramp of a fault-bend fold will yield an accurate estimate for the amount of fault slip at depth (SD). However, other classes of fault-related folds form due to fault slip gradients along a thrust ramp. In the case of a simple shear fault-bend fold (Suppe et al., 2004; Hardy and Connors, 2006), slip increases linearly up a planar ramp through the shear interval. In this scenario, measures of surface slip would likely overestimate the displacement on a deeper portion of the thrust ramp (Figure 1B). In contrast, fault-propagation folds (e.g. Suppe and Medwedeff, 1990) consume slip during thrust tip propagation, producing a linearly decreasing slip gradient up a thrust ramp (Figure 1C). If the thrust is surface-emergent, measures of surface slip would likely underestimate estimates of slip, and thus paleoearthquake magnitude or long-term slip rates. Finally, despite the wide utility of fault-related folding theories to characterize natural structures (e.g. Shaw et al., 2005), several analog and mechanical modeling studies have provided insights into natural folding deformation that cannot be described using current kinematic formulations. For example, mechanical models of fault-bend folds have been shown to accommodate shortening involving components of structural growth limb rotation, whereas the kinematic theory predicts folding exclusively by kink-band migration. These examples highlight the importance of properly defining faulting and folding relations when employing surface deformation patterns to infer fault activity at depth along thrust sheets.

In this article, we describe new methods to quantitatively relate surface faulting and surface folding strains across active thrust sheets over multiple rupture cycles. Our techniques are based on established fault-related folding concepts and new geomechanical models, which we employ to study earthquake deformation and active fold kinematics across the seismically active Southern Junggar Thrust (SJT) in the southern Junggar fold-and-thrust belt, northwest China. When combined with geochronological constraints, these methods have the ability to elucidate detailed records of fault-related folding from individual ruptures to one hundred thousand year timescales. Using high-resolution digital elevation models, subsurface seismic reflection data, and feldspar luminescence dating methods, we extract detailed records of fluvial terraces deformation and directly relate these to subsurface structure. We quantify SJT fault slip implied by Holocene fold scarps and compare these estimates to independent measures implied by Holocene fault scarp uplift records. We describe how preserved records of surface deformation can be effective tools for evaluating – and informing – interpretations of subsurface structure and folding kinematics. Finally, we define new faulting and folding relations implied by mechanical fault-related fold models to quantify fault slip from measures of terrace uplift and folding patterns. Using these techniques, we define a detailed record of fault slip and slip rate across the SJT extending from the most recent rupture in 1906 through the Late Quaternary. We establish a record of fault slip deceleration on the SJT over this timeframe, yielding one of the the most detailed records of fault slip history of any thrust sheet over a 100 kyr+ timescale.

STYLES OF ACTIVE THRUST SHEET DEFORMATION

Sediments deposited across actively growing structures (i.e. growth stratigraphy) record natural folding kinematics (e.g. Suppe et al., 1992; 1997), cumulative fault slip histories (e.g. Shaw and Suppe; 1994; 1996) and discrete coseismic events (e.g., Dolan et al., 2003; Leon et al., 2009). In a similar vein, terraces that extend across an active fold or fault can be passively deformed and record earthquake deformation from one or several ruptures. This has led to significant advancements in tectonic geomorphology utilizing deformed marine or fluvial terrace geometries to constrain active deformation (e.g. Mueller et al., 1999; Lavé and Avouac, 2000; Thompson et al., 2002; Gold et al., 2006; Scharer et al., 2006; Amos et al., 2007; Hubert-Ferrari et al., 2007; Ishiyama et al., 2007; Yue et al., 2011; Le Béon et al., 2014). These methods utilize terrace fold geometries as records of fold kinematics that can be described by fault-related folding theories, or variants of these existing methods (Figure 2). These models make different predictions for folding of growth strata or terraces that are governed by the kinematics of the underlying structure. For example, fault-bend folds (Suppe, 1983; Suppe et al., 1992; 1997) and certain classes of fault-propagation folds (Suppe and Medwedeff, 1990) grow by kink-band migration, a folding process where folds develop a constant dip and continue to widen with increasing fault slip. These kinematic models predict terrace folds to be localized across fault bends (Figure 2A-B) and above blind thrust tips. In contrast, structures that grow by limb rotation exhibit fold limbs that progressively increase fold dip with increasing fault slip. Limb rotation is a common folding mechanism in the presence of hanging wall shear (Suppe et al., 2004; Hardy and Connors, 2006; Yue et al., 2011) and is predicted across some listric fault geometries (e.g., Seeber and Sorlien, 2000; Amos et al., 2007). As a result, fault-related folds growing primarily by limb rotation produce distributed terrace fold signatures (Figure 2C-E).

An accurate classification of the deformation style present in a thrust sheet is necessary to confidently relate surface deformation to subsurface fold kinematics and fault slip at depth. In many active thrust sheets, this is not a straightforward assessment: subsurface structure – and the implied folding kinematics – must often be inferred from a combination of surface geology, subsurface geophysical data, and terrace deformation constraints. Structures that grow exclusively by kink-band migration or limb rotation yield distinct patterns of fold dips and limb widths recorded by growth strata or terraces (Figure 2). However, several records of growth strata and terrace geometries across natural structures exhibit components of both kink-band migration and limb rotation (e.g. Dolan et al., 2003; Benesh et al., 2007; Yue et al., 2011), making it difficult to discriminate between competing kinematic fold models. In addition, the ability to resolve modest differences between competing kinematic models (e.g. curved shear fault-bend fold versus listric fault-bend fold; Figure 2 D-E) with natural terraces – subject to incomplete preservation, subsequent dissection and potentially anthropogenic modifications – can prove challenging. Moreover, without independent data on fault slip and slip rate, it generally remains unclear how accurately even the most suitable of these kinematic models can be used to relate surface folding to fault slip at depth. In the following section, we describe the geologic setting of our study area – the southern Junggar basin, NW China –, which provides a unique opportunity to quantify fault slip from independent measures both folding and faulting strains over multiple earthquake cycles. We take advantage of this ideal natural laboratory for developing and applying general methods of quantifying folding across an active thrust sheet and relating it to fault slip and slip rate at depth on active thrust sheets.

SOUTHERN JUNGGAR BASIN

Structural Setting

The southern Junggar basin is the northeastern foreland fold-and-thrust belt of the Tian Shan ranges (Figure 3A). Southern Junggar is characterized by three rows of fault-related folds, which are underlain by surface-emergent and blind thrust faults (Figure 3B). Many of these structures originated as Jurassic-aged rift structures that were subsequently inverted in the Late Jurassic or Early Cretaceous (Guan et al., 2016). These inversion structures localized the development of complex fault related folds involving coeval activity on linked forethrusts and backthrusts, a class of fault-related fold termed a structural wedge (Medwedeff, 1989). Much of the Cenozoic deformation history has been localized on deep-seated detachments within the Jurassic and Cretaceous stratigraphic intervals that ramp up from their detachment levels into the cores of the wedge structures. However, most recently, the active Southern Junggar Thrust (SJT) broke through to the surface in a break-back sense of thrusting sometime in the Quaternary (Guan et al., 2016). Continued activity on the SJT has amplified the emergence of a prominent fold trend in the southern Junggar basin, composed of the Tugulu, Manas and Huoerguosi anticlines (Figure 3B), which expose Quaternary and Neogene strata along the flanks of each structure and expose Eocene rocks in the anticlinal cores (e.g. Figure 3C). These anticlines also form structural traps for petroleum fields (Guan et al., 2016), which motivated the collection of 2-D and 3-D seismic reflection data used in this study.

Seismotectonic Setting

Present-day geodetic observations suggest ~11 mm/yr of shortening is accommodated across the central Tian Shan, decreasing to ~5 mm/yr ~86° E in the southern Junggar basin and to ~0 mm/yr at ~90° E longitude (Meade, 2007). Geodetic shortening is consistent with focal mechanism solutions throughout the Tian Shan ranges (Nelson et al., 1987) and the persistence of

$M_w \geq 7$ earthquakes across the Tian Shan over the past two centuries (Molnar and Ghose, 2000). Indeed, measureable Quaternary-Holocene fault slip along discrete thrust faults throughout the ranges associated with earthquake deformation accounts for much, if not all, of the total shortening across the Tian Shan (e.g. Avouac et al., 1993; Burbank et al., 1999; Thompson et al., 2002; Hubert-Ferrari et al., 2007).

Continued fault activity throughout the Holocene on the SJT is recorded by progressive uplift of fluvial terraces across prominent fault scarps where the SJT is surface-emergent (Avouac et al., 1993; Deng et al., 1996). The SJT is a highly-segmented thrust sheet, exhibiting strike-perpendicular offsets of up to 10 km along the forelimbs of the Tugulu-Manas-Huoerguosi fold row (Figure 3B). Despite this segmentation at the surface, it has been interpreted that all three surface splays of the SJT ruptured coseismically during the most recent rupture, the 1906 M_w 74.-8.2 Manas, China earthquake (Avouac et al., 1993; Deng et al., 1996). A 3-D fault model of the SJT – constrained by 2- and 3-D seismic reflection data – reveals that, despite these significant lateral segment boundaries at the surface, the three major south-dipping surface splays of the SJT merge at depth along an Eocene detachment horizon as a continuous thrust sheet (Stockmeyer et al., 2014). The SJT extends farther to the south before ramping down below the northern Tian Shan rangefront, likely extending to the base of the seismogenic crust (Stockmeyer et al., 2014). This 3-D characterization of the SJT suggests it is capable of sourcing M_w>8 earthquakes, consistent with the magnitude estimates of the 1906 rupture.

Fluvial Terrace Records

The Tugulu-Manas-Huoerguosi folds are dissected by an internally drained fluvial system, fed by glacial melt in the northern Tian Shan. Cycles of lateral and vertical incision within several fluvial networks have produced suites of fluvial terraces throughout the basin (e.g. Figure 4A), many of which are preserved across entire fold transects (e.g. Molnar et al., 1994; Poisson and Avouac, 2004). These fluvial terraces serve as passive strain markers, recording faulting deformation where the SJT is surface-emergent as well as surface folding strains. Holocene fault activity along the SJT recorded by progressive uplift of several terrace treads was well-documented in the seminal study of Avouac et al. (1993). These records of surface faulting – recording >15 m of relief in places – were unambiguous during field reconnaissance (Figure 4B). In addition, warping of terrace treads due to distributed surface folding has been documented across the anticlinal cores of the Dushanzi and Tugulu anticlines (Molnar et al. 1994; Poisson and Avouac, 2004). These surface strains reflect subtle components of surface folding that can be readily documented. Finally, our field reconnaissance documented abrupt, localized terrace folds in the backlimb of the Tugulu fold (Figure 4C). These terraces exhibit up to hundreds of meters of structural relief, likely reflecting a significant magnitude of fault slip at depth. Thus, we have a unique opportunity to quantify deformation across the entire hanging wall of the surface-emergent SJT, from its Eocene detachment south of the Tugulu backlimb, across the core of the structure and continuing to the prominent fault scarp where the SJT is surface-emergent (Figure 3C). Quartz luminescence geochronological methods have proven well-suited for obtaining absolute age constraints for terraces across the southern Junggar basin, yielding reliable dates of terrace abandonment through the Holocene (e.g. Poisson, 2002; Poisson and Avouac, 2004; Gong et al., 2014). In this study, we apply recently developed methods of feldspar luminescence geochronology (e.g. Brown et al., 2015; Rhodes, 2015) that extend the range of reliable ages for terrace abandonment to the Late Quaternary.

An Ideal Natural Laboratory

The southern Junggar basin presents a unique opportunity to apply quantitative methods of extracting thrust sheet deformation and natural fold kinematics from records of active terrace faulting and folding. Specific aspects of the study area that produce such a unique location include: 1) an active thrust sheet that ruptures in large earthquakes, likely $M_w \geq 8$; 2) the availability of high-quality 2- and 3-D seismic reflection data imaging subsurface fault geometries and folding kinematics; 3) several records of both surface faulting and surface folding strains, captured by deformed fluvial terrace records across the entire hanging wall of the active thrust sheet; and 4) the ability to obtain reliable, absolute age constraints of surface strain markers to constrain fault slip rates over >100 kyr timescales.

SUBSURFACE DEFORMATION

The Southern Junggar Thrust (SJT) is thought to be the most active structure in southern Junggar; it most recently ruptured during the 1906 M_w 7.4-8.2 Manas, China earthquake (Avouac et al., 1993; Burchfield et al., 1999). Due to active petroleum exploration and development in the region, the SJT and hanging wall fold geometries are well-constrained by high-quality 2- and 3-D seismic reflection surveys (Stockmeyer et al., 2014; Guan et al., 2016). The SJT is particularly well-imaged in the upper 3-4 km of the crust due to the presence of direct footwall cutoffs, terminating hanging wall axial surfaces, and direct fault plane reflections (Stockmeyer et al., 2014). These data provide tight constraints on the geometry and location of each segment of the SJT. Our interpretation of the SJT in section A-A' (Figure 5) depicts the thrust sheet stepping up from its mid-crustal Eocene detachment (Stockmeyer et al., 2014). This Eocene detachment has a modest dip of 3.4° ± 1.5° south (θ_0). The SJT rises from this detachment across multiple synclinal fault bends, achieving a dip of 27.4° ± 1.5° south (θ_2). To generate this steeper ramp dip, we interpret three principal fault bends that are associated with synclinal axial surfaces in the hanging wall strata. The axial surfaces for the latter two bends interfere in the near-subsurface producing a single axial surface trace representing the transition from the fault segments labeled θ_1 to θ_2 in Figure 5 (e.g. Medwedeff and Suppe, 1997). The relationship of this fault geometry to the hanging wall folds is consistent with classic fault-bend folding theories (Suppe, 1983; Medwedeff & Suppe, 1997). Another viable interpretation for this 24° increase in fault dip could invoke a curved fault geometry (Suppe et al., 1997). The well-defined planar geometries for the detachment (θ_0=3.4°) and the thrust ramp beyond the bend (θ_2=27.4°) observed in the 2D and 3D seismic data limit the horizontal extent of this zone of curvature to a maximum dip-parallel distance of ~2000 m. In such a case, the axial surfaces accommodating folding in the hanging wall would have a comparable finite width (Suppe et al., 1997). In either case, terrace deformation caused by displacement across these fault bends is expected to occur along – or at least in the vicinity of – surface projections of active synclinal axial surfaces (Figure 2A-B; Shaw et al., 1994). A third interpretation we explored invoked a listric fault-bend fold interpretation (e.g. Figure 2E; Seeber and Sorlien, 2000; Amos et al., 2007). We document why such an interpretation is not viable for the SJT in Appendix A.

Farther to the north in section A-A’, we interpret the SJT further increases its dip across a series of fault bends associated with synclinal axial surfaces in the hanging wall stratigraphy (Figure 5). We observe direct fault plane reflections indicating that the SJT branches into two fault splays across this series of fault bends. The northern surface splay of the SJT has a strictly planar geometry and is surface-emergent where Avouac et al. (1993) documented a prominent fault scarp in the Taxi He valley (Figure 5). This finding has two primary implications. First, the planar geometry of the SJT across the structural crest of an underlying imbricated structural wedge (Figure 5) implies the SJT is the only active structure at present (Lu et al., 2010; Guan et al., 2016), and thus, all terrace deformation is due to fault-bend folding along the SJT. If the deeper structures were active, the shallow segments of the SJT would be folded where they cross the footwall fold crest. This is the primary evidence to suggest the SJT reflects a period of break-back thrusting regionally across the southern Junggar thrust belt (Guan et al., 2016). Second, as there is only a fault scarp across the northern surface trace of the SJT, the near-surface splays of the thrust sheet appear to have developed in a locally break-forward sequence of thrusting. The lack of any differential uplift across the southern surface splay of the SJT implies it has been inactive since at least the start of the Holocene. In addition, this suggests the black axial surface in Figure 5 is inactive; we should not expect any terrace deformation across the surface projection of this synclinal axis. Thus, our detailed constraints on SJT fault activity reflect a complex evolution of thrusting sequences. Regionally, the SJT reflects break-back thrusting as it truncates older, inactive structures in its footwall. Locally, however, near-surface splays imply a break-forward thrusting sequence. This complex thrusting sequence adds to the structural complexity of the southern Junggar fold-and-thrust belt (Guan et al., 2016). However, our subsurface interpretations yield a rather straightforward expectation for our records of surface deformation: any terrace folding can be attributed to fault slip on the SJT across active (i.e. green) axial surfaces and terrace faulting should be exclusive to the northern surface splay (Figure 5). Thus, records of surface deformation can be used as a rather effective tool to evaluate our subsurface interpretations of fault-bend folding, regional break-back thrusting (Guan et al., 2016) and local break-forward thrusting at Tugulu (Figure 5).

Altogether, we interpret the SJT as a series of south-dipping fault ramps that increase in dip from 3.4° ± 1.5° (θ_0) along its Eocene detachment to 44.5° ± 1.5° (θ_4) at the surface (Figure 5). The planar geometry of the SJT splays across the crests of the footwall anticlines indicates the deeper structures are inactive. The fault bends along the active segments of the SJT yield active synclinal axial surfaces, which, when projected to the surface, provide locations where surface folding is expected to occur (e.g. Shaw et al., 1994), if our interpretations of fault-bend folding and thrusting sequences are accurate. Similarly, terrace uplift from surface faulting is predicted to be limited to the northern SJT surface trace, which would be consistent with our thrust sequence interpretation and the work of Avouac et al. (1993). In the following section, we assess our subsurface interpretation by comparing terrace deformation to the predictions implied by our subsurface interpretation (e.g. Figure 2A). We then quantify fault slip using terrace folds and compare these to slip estimates implied by the fault scarp record. In this way, we seek to validate the method of using surface fold relief to quantify fault slip by establishing a direct comparison to independent slip constraints from the fault scarp. Moreover, we continue to critically evaluate our subsurface interpretation of fault-bend folding by comparing fault slip gradients across the SJT implied by the terrace deformation to the predictions from fault-bend fold theory (Figure 1A).

SURFACE DEFORMATION

Terrace Mapping with High-Resolution Topographic Data

Preserved terraces along the Taxi He valley have recorded localized and distributed deformation across the SJT (Avouac et al., 1993; Molnar et al., 1994; this study). We acquired a 5-m vertical resolution digital elevation model across the Taxi He Valley to correlate terraces across the entire transect of the Tugulu fold (Figure 3C). The vertical resolution was improved to 70 cm using 10 differential Global Position System (dGPS) ground truth points. This high-resolution topographic data is capable of precisely defining fault uplift and folding signatures across the entire hanging wall of the SJT over multiple rupture cycles. Based on field observations and various methods of interpreting fluvial terraces (e.g. location, elevation, geometry) we mapped seven distinct terraces in the topography data across the Taxi He valley (Figure 6A). In our study, T6 is the youngest mapped terrace and T0 is the oldest. The youngest of these (T4-T6) are present across the entire transect of the thrust sheet, providing three records of both surface folding and surface faulting. Younger terraces are present in isolated remnant locations throughout the valley, but are too discontinuous to confidently correlate over large distances of non-preservation. One of these terraces, T8, provides a lower age constraint for T6. The older terraces (T0-T3) are less continuous, limited to the southernmost dip domains (θ_0-θ_2) along the SJT. However, these markers exhibit significant uplift and folding deformation, providing a long record of SJT fault slip activity.

In subsequent sections, our structural analyses consider residual terrace profiles, which have had their original depositional gradients removed (Figure 6B-C). A brief description of how we mapped terraces and removed the original depositional gradients is provided in Appendix B. We document our assessment of uncertainties related to measurements used to quantify fault slip (e.g. terrace elevation, fault dip) in Appendix C. We note that the loess cap, which often defines terrace treads in southern Junggar (e.g. Figure 4C), has been completely eroded from our T0 terrace, suggesting T0 has undergone at least modest amounts of erosion. Thus, any measure of fault slip implied by our T0 profile reflects a minimum estimate of SJT slip since the time of T0 abandonment.

Terrace Geochronology

Ages of terrace abandonment are required in order to obtain rates of surface deformation and associated fault slip rates. Luminescence geochronological methods have proved capable of obtaining reliable absolute age constraints for the lower-elevation terraces across southern

Junggar, analogous to our T4-T6 terraces (e.g. Poisson, 2002; Poisson and Avouac, 2004; Lu et al., 2010a; Gong et al., 2014). We employ the recently developed single-grain, post-infrared, infrared stimulated luminescence (p-IR IRSL) methods (Buylaert et al., 2009; Thiel et al., 2011; Brown et al., 2015) to date fluvial deposits in each terrace used for our structural analysis. Fluvial deposits are composed of very fine grain to boulder sized clasts. In most locations, the fluvial deposit is overlain by a light tan loess cap. For each terrace we collect 2-5 samples at least 25 cm below the loess cap by driving a 150 mm aluminum tube into the fluvial deposit and capping the ends of the full tube, shielding the inner 15 cm of sample from exposure to sunlight. Samples for T0-T6, T8 terraces were collected in the backlimb of the Tugulu fold with an additional set of samples collected for T4 near the fault scarp in the forelimb of the fold (Figure 3C).

K-feldspar grains were isolated from the sedimentary samples under dim amber light conditions. Samples were wet-sieved to and treated with low-concentration (3%) HCl. The 175-200 μm diameter size fraction was then separated according to density with lithium metatungstate to extract the most K-rich feldspars ($\rho < 2.565$ g/cm^3; Rhodes, 2015). Finally, the grains were treated with dilute HF for 10 min to remove the outer surface and enhance grain brightness.

All luminescence measurements were performed on a TL-DA-20 Risø automated luminescence reader equipped with a single-grain IR laser and a $^{90}Sr/^{90}Y$ beta radiation source (Bøtter-Jensen et al., 2003). Emissions were detected through a Schott BG3-BG39 filter combination. Grains were mounted on aluminum discs, seated within 100 holes per disc.

Small (10 g) portions of the bulk sediment were measured with inductively-coupled plasma mass spectrometry (ICP-MS) and inductively-coupled plasma optical emission spectrometry (ICP-OES) to measure the U, Th, and K concentrations. These values were used to determine the annual beta dose-rate following the conversion factors of Adamiec and Aitken (1998). An internal potassium content of 12.5 ± 0.12 wt% was used to calculate the internal dose rate (Huntley and Baril, 1997). The outer edges of sediment taken from sample tubes were oven dried to determine the water content of samples. Cosmic dose-rates were estimated based on overburden depth and geomagnetic latitude after Prescott and Hutton (1994).

To avoid problems associated with signal fading in K-feldspar sediments (e.g., Huntley and Lamothe, 2001), we measure both the initial IRSL signal at low temperature and also a subsequent high-temperature, post-IR IRSL signal, which has been shown to be more stable (Buylaert et al., 2009). We measure the p-IR IRSL signal at a temperature of 225 °C (preheat of 250 °C for 60 s) to measure the charge population which is both bleachable by sunlight exposure and stable through time (Smedley et al., 2015). Single-aliquot regenerative (SAR) dose-response curves (Murray and Wintle, 2000) were measured for each grain to determine the total radiation dose required to produce the natural luminescence signal (i.e., the equivalent dose, D_e).

By dividing the equivalent dose by the natural dose-rate, we calculate an approximate age of that grain. If the grains within a sample show a sufficient degree of internal consistency (i.e., overdispersion less than about 20 ± 9 %; Arnold and Roberts, 2009) there are interpreted as comprising a single dose-population and an age model (e.g., Central Age Model or Minimum Age Model; Galbraith et al., 1999) is used describe the age of terrace abandonment. However, sediment grains from a single sample often exhibit a range of De values. In the case of our samples, none of the 26 samples exhibited enough internal consistency to be interpreted a single, well-bleached population.

To reduce the uncertainties in the depositional ages for these terraces, we adopt a Bayesian approach which uses our prior knowledge of terrace depositional order to impose the condition that each uplifted terrace must be the same age or older than the terrace beneath it. The use of stratigraphic order for refining depositional age models is common in archaeological studies (Litton and Buck, 1995) and since the advent of the OxCal software program (Bronk Ramsey, 1995) Bayesian statistics are routinely applied in the interpretation of radiocarbon ages. More recently, geologists have begun to incorporate this technique to interpret luminescence ages of samples with definite stratigraphic relationships (Rhodes et al., 2003; Greenbaum et al., 2006; Cunningham and Wallinga, 2012; Brill et al., 2015). While efforts are underway to develop a full incorporation of measurement errors, systematic errors, and dose-rate uncertainties into a Bayesian framework for luminescence studies (e.g., Combès et al., 2015), the use of stratigraphic order as a Bayesian prior applied to the interpretation of single-grain luminescence ages is largely undeveloped.

First, for every terrace we construct a summed probability distribution. The natural logarithm of every single-grain age value is set as the mean of a Gaussian distribution, and the relative standard error is used for the standard deviation of this distribution. By adding all single-grain distributions together, we construct our log-transformed probability distribution of all single-grain ages within a given terrace (Figure 7). This distribution represents the depositional age probability for each terrace individually, before considering stratigraphic order. Second, we randomly select one of the terraces (T0-T6, T8). The age of this terrace is sampled from its prior age distribution. From this initially-chosen terrace, we must move stratigraphically up and down until all terraces have been assigned ages. If a sampled terrace age is stratigraphically consistent, the age is accepted; if not (e.g. T5 > T4), another age is chosen. This continues until a stratigraphically consistent age is given to each terrace or a pre-determined number of iterations is exceeded. We run 10,000 simulations which are fitted to produce a posterior age distribution for each terrace from all successful model simulations (Figure 7).

The posterior age probabilities exhibit modest overlap at the 1σ level (Figure 7) The posterior procedure described above has an implicitly defined lower-bound for terraces ages of present-day but does not contain a similar, upper-limit. This yields greater age control for Holocene aged-terraces (Figure 7). The single-grain ages of older terraces (T0-T3) have higher standard deviations, and precision remains low even after incorporating stratigraphic constraints. Moreover, the use of relative standard errors instead of absolute errors produces asymmetric standard deviations that positively skewed (Figure 7).

Fault Slip Estimates from Surface Deformation

Surface Faulting

As documented by Avouac et al. (1993), there is a prominent fault scarp delineating the surface trace of the active SJT splay along the forelimb of the Tugulu anticline. The surface fault dip slip (u_j) required to produce the observed amount of terrace uplift relative to the footwall position (h_j) is given by:

$$\boldsymbol{u_j = \frac{h_j}{\sin\theta_j}} \qquad (1)$$

where θ_j is the dip of the underlying fault segment relative to horizontal, measured in degrees, and h_j is the total structural relief above dip domain j, given by:

$$\boldsymbol{h_j = z_j - z_{fw}} \qquad (2)$$

where z_x is the elevation of the unfolded terrace within dip domain j, and z_{fw} is the footwall elevation of the terrace (Figure 8).

Surface Folding

Actively uplifting structures often do not have a preserved record footwall terraces due to footwall aggradation (Lavé and Avouac, 2000; Yue et al., 2011; Le Béon et al., 2014). Without a footwall level, estimates of fault slip from surface faulting require assumptions about base level changes and sedimentation rates to estimate the burial depth of the footwall terrace relative to the present-day stream bed. This method has been shown to yield reasonable estimates of fault slip when base level changes have been considered thoroughly (e.g. Lavé and Avouac, 2000). However, the traditional method of quantifying fault slip from surface fault uplift by (1) can be generalized to yield estimates of fault slip at depth from fold scarps or fault scarps. This method is independent of base level changes when applied to fold scarps (e.g. Yue et al., 2011; Le Béon et al., 2014), avoiding additional uncertainties associated with estimates of z_{fw} if a terrace is not preserved in the footwall (e.g. e.g. Lavé and Avouac, 2000). The structural relief produced across two dip domains, i and j, provides an estimate of slip by:

$$\boldsymbol{u_j} = \frac{\Delta \boldsymbol{h_{ji}}}{\sin \boldsymbol{\theta_j} - \sin \boldsymbol{\theta_i}} \qquad (3)$$

where

$$\Delta \boldsymbol{h_{ji}} = \boldsymbol{z_j} - \boldsymbol{z_i} \qquad (4)$$

The generalized forms in (3) and (4) reduce to (1) and (2) when dip domain i refers to the footwall of the fault (i.e. $\theta_i = 0°$). The generalized formula for quantifying fault slip from terrace relief in (3) is applicable across one or multiple fault bends across a thrust sheet; j-i need not equal 1. Thus, if a thrust sheet has several fault bends, such as the SJT (Figure 5), (3) may yield several estimates of fault slip.

We have precise constraints on the footwall positions of the Holocene terraces, T4-T6 (Figure 6B), but the Quaternary terraces, T0-T3, are only preserved as fold scarps (Figure 6C). In the following section, we test the accuracy of (3) for estimating magnitudes of fault slip from only fold scarp relief by directly comparing it to measures of fault slip implied by the fault scarps using (1).

INTEGRATED RECORDS OF ACTIVE THRUST SHEET DEFORMATION

Holocene Fault Activity

Fault Scarp Estimates of Fault Slip

Structural relief of the T4 terrace across the Taxi He fault scarp suggests ~15 m ± 1.2 m of vertical throw on the SJT (Figure 6B) since it was abandoned in the early Holocene (Figure 7). The progressive decrease in structural relief with decreasing terrace age implies a record of multiple rupture events on the SJT throughout the Holocene. We use (1) to calculate total fault slip on the SJT since the time of terrace abandonment for each Holocene terrace and our constraints of subsurface fault dip to (Table 2). This surface faulting record suggests at least 21.4 m ± 2.4 m of fault slip on the SJT during the Holocene.

Fold Scarp Estimates of Fault Slip

We calculate the fault slip required to produce the measured structural relief across all possible combinations of dip domains for the T4-T6 using (3). As discussed above, our interpretation of the SJT geometry and its hanging wall fold reflects fault-bend folding (Suppe, 1983). For our case of ~parallel hanging wall strata and underlying fault dip, fault-bend folding predicts no change in slip across a synclinal fault bend (Suppe, 1983). Therefore, we should expect a single magnitude of fault slip to explain all of our measures of structural relief and change in fault dip used in (3) for a given terrace. In Figure 9A, we plot structural relief versus change in fault geometry and apply a linear regression to each terrace dataset that runs through the origin, reflecting no relief for no slip. The slope of each best-fit function yields the magnitude of slip that best describes the terrace fold scarps and fault dip data. The low variance between the linear models and the data implies no change in fault slip across the entire hanging wall of the SJT among the fold scarps (Figure 9A), indicating that a single magnitude of fault slip can readily explain all of the observed fold scarps for each Holocene terraces (T4-T6).

The fold scarps preserved in the T5 record yield consistent fault slip values across dip domains x=0, 3 and 4 (Figure 9A). We note that the uplift preserved across the T5 fold scarps corresponding to dip domains 1 and 2 is less than the relief preserved for T6 in the same dip domains (Figure 6B). As T5 is older than T6 in both an absolute (Figure 7) and relative (Figure 6A) sense, T5 must have experienced at least as much fault slip as T6. However, the regions where relief is greatest suggests T5 has been deformed by more SJT fault slip than T6 (Figure 6B), consistent with the result from the fault scarp data (Table 2). This suggests some of the uplift experienced by T5 has been removed in dip domains 1 and 2. Potential mechanisms to remove terrace fold relief may require lateral erosion, perhaps slake-driven lateral incision (Johnson and Finnegan, 2015), or, if the Taxi He was transporting sufficiently erosive bedload at that time, downstream sweep erosion (Cook et al., 2014). Whatever the mechanism may have been, the consistency of fault slip suggested by all of the slip measures by T4 and T6 as well as the T5 data used in Figure 9A suggest the two depressed uplift signals in the T5 profile are likely underestimating total SJT fault slip.

When we compare the magnitudes of fault slip derived using (1) and (3) using the fault scarp and fold scarp data, respectively, the results are indistinguishable (Figure 9B). This is further consistency with our fault-bend folding interpretation for the hanging wall of the SJT. A linear regression to these data suggest a fairly constant Holocene slip rate on the SJT of 1.2-1.3 mm/yr (Figure 9B).

We have established that quantifying fault slip from terrace folds can accurately reflect total fault slip at depth (Figure 9). We suggest this provides confidence for using folding recorded by growth strata or terraces to quantify fault slip on blind thrust sheets (e.g. Dolan et al., 2003; Benesh et al., 2007). When possible, seismic hazards assessments should employ this method using as many different measures of fold relief as available in order to evaluate the potential for spatial gradients in slip along an active thrust sheet (e.g. Figure 1). In our case, a fault-bend fold, we can state confidently that a single measure of fault slip anywhere in the hanging wall would have been yielded an accurate measure of fault slip at depth. Yet, we could not have stated this with confidence if we only used a single fold scarp in our analysis. We only validate the lack of slip variation by producing a complete record of surface folding and surface faulting deformation across the entire SJT in our study area.

Quaternary Fault Activity

The T0-T3 terraces provide a record of Late Quaternary surface folding across the Tugulu backlimb (Figure 6C; 7). While the Holocene terraces would only record a few earthquakes equivalent to the 1906 Manas, China event, these older terraces provide long-term records of uplift due to fold growth and fault activity on the SJT – likely the products of hundreds of 1906-equivalent ruptures. Given the discontinuous nature of these older terraces, they do not record fault offset. Therefore, we use (3) to constrain the fault slip required to produce the observed fold relief for T0-T3 (Table 3). The z_0 elevation – the residual elevation above the detachment – for both T2 and T3 is preserved in our terrace records (Figure 6C). To estimate z_0 for T1 and T0, we assume the rate of incision implied from T2 to T3 has been constant since the abandonment of T0. Although we do not have evidence for a constant incision rate from ~250-100 ka, this method should yield a reasonable approximation for the structural relief developed before T1 abandonment. As described previously, the magnitude of fault slip from the T0 profile is likely a minimum constraint, given the evidence for erosion. Our calculations from (3) suggest a minimum of ~525 m of fault slip on the SJT over the past ~250 kyr (Table 3). Before we discuss the long-term slip rate history on the SJT implied by our terrace data, we discuss the folding kinematics implied by the T0-T3 terrace geometries (Figure 6B), which appear to deviate from the predictions of kinematic fault-bend fold theories (Figure 2A-B). In doing so, we attempt to develop a method for quantifying fault slip from terrace fold dips, which, if successful, will provide a more accurate estimate for fault slip implied by the T0 terrace profile.

Quaternary Terrace Fold Kinematics

The Quaternary terraces preserved across the backlimb of the Tugulu fold exhibit a fanning of limb dips, with older terraces dipping more steeply than younger terraces (Figure 6C). Where preserved, these terraces acquire their dips over a region of finite width, coincident with synclinal axial surfaces that reflect the SJT increasing its dip from 3.4° to 27.4°. The variable limb dips exhibited by these Quaternary terrace folds are remarkably planar. These observations suggest T0-T3 folds have developed – at least in part – by limb rotation. Limb rotation is a folding mechanism that describes fold limbs which progressively increase their dip with increasing fault slip. Fault-bend folding theories (Suppe, 1983; Suppe et al., 1997) predict these structures grow exclusively by kink-band migration (Figure 2A-B). Kink-band migration is a folding mechanism whereby folds acquire a constant dip after passing over a fault bend – instantaneously (Figure 2A) or over some region of finite width (Figure 2B) – and widen at this constant dip with increasing fault slip.

Observations of progressive limb rotation across fault-related folds have led to the development of numerous fault-related fold variants based in part on the original fault-bend fold theory. These commonly invoke an axial surface zone of some finite width (e.g. Erslev, 1986; Suppe et al., 1997; Seeber and Sorlien, 2000), and may invoke additional folding mechanisms that involve limb rotation, such as trishear (Erslev, 1993; Allmendinger, 1998; Cristallini and

Allmendinger, 2002; Brandenburg, 2013). Simple and pure shear fault-bend folding models describe structures that grow by a combination of kink-band migration and limb rotation (Suppe et al., 2004; Hardy and Connors, 2006).

More recently, studies have explored the possibility that structures may deviate from the strict kinematics of fault-bend folding theory under certain conditions (Benesh et al., 2007; Benesh, 2010). These studies have employed mechanical forward models using the discrete element modeling (DEM) technique. These models readily produce fault-bend folds that grow by a combination of kink-band migration and limb rotation – referred to herein as hybrid folding– as strata are displaced across a discrete fault bend (Benesh et al., 2007; Benesh, 2010). This behavior offers the prospect of reconciling our observations that Holocene slip on the SJT is consistent with fault-bend folding kinematic predictions of slip magnitudes across the entire hanging wall (Figure 1A, 5, 9B) while the fanning of limb dips in the Quaternary terrace record implies a component of folding by limb rotation (Figure 6C).

A MECHANICAL MODEL OF THRUST SHEET DEFORMATION

Model Description

Following the work of Benesh et al. (2007) and others (e.g., Strayer et al., 2004; Benesh, 2010; Hughes and Shaw, 2015; Morgan, 2015), we produced a mechanical model of deformation within a thrust sheet using a discrete element model (DEM) to help guide our interpretations of folding kinematics for the hanging wall of the SJT, including the T0-T3 terraces. The DEM method is able to replicate natural brittle-plastic deformation processes such as folding, frictional sliding, fracture growth, and the influence of mechanical stratigraphy (e.g., Cundall and Strack, 1979; Morgan, 1999; Strayer et al., 2004) that likely influence the manner of deformation during natural fault-related folding. We created our model using the 2-D Particle Flow Code (PFC) numerical modeling package, which describes granular behavior of linear elastic particles with frictional contacts. The code employs a method by which circular balls interact at an infinitesimally small contact. These contacts can replicate both shear and tensional bonding between particles. If bonds are broken, balls will interact and can slide, governed by Coulomb frictional sliding behavior. In addition, physical rock properties such as density, elastic moduli, and friction can be prescribed. Moreover, forces are implemented to models, such as gravity and translating boundary walls. Translating walls are often employed as displacement boundary conditions to drive deformation. For a more detailed description of the DEM method and PFC code applied to studies of active deformation and folding kinematics, we direct the reader to Benesh (2010); Hughes et al. (2014); and Morgan (2015).

We define a 24° dip change along the fault in our mechanical model to replicate folding of the T0-T3 Quaternary terraces across the SJT, where they are preserved (e.g. Figure 5, 6C). The model includes a 12 km long detachment that steps up to a thrust ramp dipping 24° (Figure 10A). We deposit pre-growth strata to the hanging wall of our fault model in 500 m thick layers, following the same settling procedure of Benesh et al. (2007), allowing each layer to reach a state of static equilibrium following deposition. Between pre-growth layers, we deposit 125 m thick sections that have smaller ball radii, no friction and lack bonding. These weak layers are employed to promote flexural slip during deformation, which enables the structure to deform in a manner consistent with fault-bend folding (Suppe, 1983; Benesh, 2010). We deposit seven layers of pre-growth and six flexural slip surfaces (Figure 10A). A boundary condition is applied to the leftmost boundary wall to translate along the detachment fault at a constant rate of 1 m/s. After each 250 m interval of fault slip, we deposit a layer of growth strata to a thickness that is 100 m higher than the mean elevation of the structural crest. Growth strata aid in recording the kinematics of the fold growth and also serve to limit effects such as slumping and minor extension that can develop at the top of the hanging wall. The material properties prescribed for our model are summarized in Table 4.

There are many similarities between our mechanical model result and kinematic fault-bend fold theory (Suppe, 1983). In the final state of deformation (Figure 10B), pre-growth strata parallel the underlying thrust ramp, which is the kinematic prediction for our initial model geometry. As a result, slip on the fault ramp is generally constant and consistent with the structural relief across the fold in its hanging wall. This behavior further validates (3) to calculate slip on the SJT from the fold scarp relief of deformed terraces. In the growth strata of our model, we observe a narrowing upward growth triangle (Figure 10B), which is diagnostic of fold growth by kink-band migration - the mechanism invoked by fault-bend folding theory (Suppe et al., 1992; Shaw and Suppe, 1994). However, we observe additional details that reflect important departures from the kinematic expectations, consistent with similar studies (Benesh et al., 2007). Most notably, there is a shallowing upward of limb dips in growth strata, suggesting the hanging wall has deformed by a component of limb rotation. Moreover, we observe a distributed zone of folding that has developed to accommodate fault slip across the discrete bend in the thrust sheet at depth. This results in a much wider region of folding than generally is described by the kinematic theory.

Our mechanical fault-bend fold model accommodates shortening during structural growth in part by limb rotation (Figure 10B). Thus, the fanning of dips exhibited by T0-T3 (Figure 6C) remains consistent with fault-bend folding when stresses and mechanical stratigraphy are considered. To quantify how bed dips evolve in the model, we record fold dip and total slip experienced for each bed in both growth and pre-growth sections following each 250 m slip interval. For each strata type, we calculate the average dip for a given amount of fault slip (Figure 11A). We find that both pre-growth and growth layers develop their dips incrementally (Benesh, 2010), reflecting a component of fold growth by limb rotation throughout the hanging wall of our mechanical fault-bend fold model (Figure 11A). This pattern of dip evolution was a robust feature for growth and pre-growth strata in all of the models we tested. We find that these relationships are generalized by a second-order polynomial functions that passes through the origin, reflecting zero slip and dip (Figure 11A). The precise nature the dip evolution – governed by the two constants in the functional form – will vary as a function of layer strength, thickness, and the spacing of flexural slip surfaces. However, all of the models we tested – in addition to those of Benesh et al. (2007) and Benesh (2010) – involve a component of fault-bend folding by limb rotation in both growth and pre-growth strata, similar to the implied kinematics of the T0-T6 terraces in our study area (Figure 5, 6, 9).

Deriving Fault Slip from Terrace Dips

The pre-growth strata generally develop folds much faster than growth strata in this DEM approach (Benesh et al., 2007). In addition, variations in mechanical stratigraphy of a DEM model can yield changes in the precise form the quadratic dip-slip functional relation described above. This variability presents a challenge for determining the appropriate way to relate bed dips to fault slip in natural structures, given that we generally lack precise knowledge of these mechanical properties. Thus, we suggest an approach that employs fitting a second-order polynomial function to data from the natural structure. Specifically, terraces that preserve both limb dip and structural relief can be used directly in this fitting procedure. For the SJT, this information is available for the T1-T4 terraces (Figure 6). We omit T0 from the fitting procedure due to the potential it has undergone significant erosion, as described above. In addition, we supplement our natural terrace dataset with an upper constraint on the critical slip value required to produce the maximum allowable dip, which in our model and the SJT is limited by the ramp dip. The critical slip for the SJT is constrained by pre-growth fault offset across the SJT to be ~2800 m (Guan et al., 2016; their Figure 4). Thus, the Tugulu pre-growth strata require no more than ~2800 m of fault slip to achieve their maximum dip. By incorporating this critical slip and maximum pre-growth dip relation, along with the other direct constraints from terraces that preserve both dip and uplift, we suggest that it's possible to develop a robust relationship between terrace dip and slip.

We note that growth strata may have a different critical slip than pre-growth, as discussed above (Figure 11A). However, terraces are merely passive strain markers. Thus, it seems reasonable that they will be governed by the dip-slip relation of whichever stratigraphic interval they reside within. In our case, the SJT has incised into the pre-growth strata, leaving behind terraces within the Tugulu pre-growth section. Thus, we suggest the pre-growth critical slip value serves as an effective constraint for our terrace data. Our work here, as well as that of Benesh (2010), consistently found that growth layers acquire fold dips more gradually than pre-growth. Thus, magnitudes of fault slip we define by the functional form derived using the pre-growth critical slip value will yield a minimum slip estimate for the terrace data. This reflects uncertainty in how the mechanical stratigraphy of the fluvial deposits overlying the pre-growth may fold precisely. Regardless of this effect, it's reasonable to suggest the pre-growth critical slip is not greater than the critical slip for the terrace folds.

We define a dip-slip relationship for the Quaternary folds in the backlimb of the Tugulu structure. The constraints for this relationship include dip and slip for the T1-T4 terraces, the pre-growth strata, and the origin, with the origin reflecting no dip for zero fault slip. The functional form of the 2nd-order polynomial describing the terrace dip-slip relation yields a tight fit to the data, suggesting it is a viable path to describe the history of fold growth for the terrace data. In addition, this dip-slip relation confirms our observation that the slip derived from the T0 structural relief will underestimate total slip. However, we can use the observed T0 dip magnitude to estimate the total amount of slip that has occurred on the SJT since the time of T0 abandonment (Figure 11B). Finally, the tight fit to the terrace data using the pre-growth critical slip magnitude implies that this is a reliable measure for the critical slip for our terrace folds.

We conclude the slip estimates from uplift of Holocene terraces (T4-6) – which are consistent with kinematic fault-bend fold theory (Suppe, 1983) – can be reconciled with the fanning of limb dips in Quaternary terraces (T0-T3) – which deviate from kinematic fault-bend fold theory (Suppe, 1983) – through a mechanical fault-bend fold model that grows by a combination of limb rotation and kink-band migration (Figure 11B). We do not advocate that any specific mechanical model can be used to uniquely define the dip-slip relation for a specific natural structure. In contrast, we suggest that the general functional form of this relationship can be effectively described by a second-order polynomial relation that fits through the origin. This offers a generalized approach by which limited data from natural folds – surface folds or buried growth strata– may be used to develop a quantitative relation between fold geometry and fault slip at depth (Figure 11).

250 KYR RECORD OF ACTIVE THRUST SHEET DEFORMATION

Based on our analysis of the kinematics governing the dip-slip relation for the hanging wall of the SJT, the slip estimates derived from (3) for the T4-T6 terraces, and our new terrace geochronology (Figure 7), we have developed a detailed history fault slip rate on the SJT (Figure 12). Specifically, the mean slip rate for the SJT has decelerated from a maximum of ~7.0 mm/yr in the Late Quaternary, to a mean slip rate of ~1.3 mm/yr throughout the Holocene (Figure 9; 12). We formally evaluate this conclusion of a decelerating SJT slip rate from the Late Quaternary to the Holocene by performing an f-test on the functional forms fit to the terrace data that considers uncertainties in our estimates of fault slip as well as the terrace age uncertainties (Appendix C). In this assessment, a 2nd-order polynomial function fits our terrace data more accurately than a constant slip rate (i.e. linear) function fit to all of the data (Supplemental Figure C1). Thus, although the actual SJT slip rates may differ from the preferred values reported here within the range of our uncertainties, our conclusion of a decelerating slip rate from the Late Quaternary to the Holocene remains robust.

Our preferred Holocene slip rate represents ~25% of the geodetically measured shortening across the Tian Shan rangefront at the 86° latitude of our studied area (Meade, 2007). Thus, the SJT currently serves as a principal structure for accommodating shortening across the eastern Tian Shan in. A faster slip rate on the SJT in the Late Quaternary implies: 1) the regional shortening rate has decreased over the past 250 kyr, 2) deformation formerly accommodated on the SJT has shifted to structures toward the hinterland, within the Tian Shan ranges, or 3) a combination of 1 and 2. Moreover, the dynamic history of SJT slip rate suggests that single measures of fault slip rate for active thrust sheets may not be adequate to properly characterize past or present-day slip rates. Thus, in addition to considering spatial slip gradients in thrust sheets (Figure 1), adequate seismic hazards studies should consider temporal variations as well (Figure 12).

CONCLUSIONS

Through a unique case study integrating deformed fluvial terraces, feldspar luminescence geochronology, and structural analysis facilitated by seismic reflection data and mechanical forward models, we have developed a new method of extracting detailed histories of fault slip and slip rate from folds in thrust sheets. By combining kinematic and mechanical modeling methods, we developed quantitative relationships between fold relief, fold limb dip, and slip that enabled us to extract a ~250 kyr history of deformation and fault activity on the SJT from measures of terrace fold dip and uplift. These methods can be readily employed in regions of active convergent tectonics to delineate active thrust faults, growing folds, and, thus, understand their histories of deformation over multi-rupture timescales. Moreover, methods that consider more complete records of deformation over multiple rupture cycles provide unique insights into the mechanisms of natural fold growth in relation to thrust faulting. With proper consideration of the potential for spatiotemporal fault slip variations (e.g. Figure 1, 12), hazards assessments can provide more accurate details of fault activity, paleoearthquake magnitudes, and slip rates to better reduce the risk to life and property in active thrust belts.

APPENDICES

Appendix A: Evaluating Alternative SJT Kinematic Models

We present our preferred interpretation of the SJT fault bend from its Eocene detachment (θ_0=3.4°) to a steeper planar ramp dip (θ_2=27.4°) in Figure 5. In this interpretation, we follow classic fault-bend folding (Suppe, 1983; Medwedeff and Suppe, 1997) where folding occurs across an instantaneous change in fault dip and axial surfaces bisect the hanging wall syncline fold. An equally permissible interpretation allows for a curved-hinge fault bend fold (e.g. Suppe et al., 1997) that progressively increases the fault dip over a ~2,100 m zone of finite width. A third possibility is a listric fault-bend fold (Seeber and Sorlien, 2000; Amos et al., 2007). This possibility has important implications on the expected folding kinematics as listric fault-bend folds develop by limb rotation (Figure 2E) whereas either of the viable fault-bend fold models deform by kink-band migration (Figure 2A-B).

In listric fault-bend fold kinematic model (Seeber and Sorlien, 2000), entry and exit axial surfaces are oriented perpendicular to the entry (e.g. θ_0=3.4°) and exit (e.g. θ_2=27.4°) thrust fault dips. These axial surfaces meet at a point in the hanging wall of the thrust sheet, defining the origin and radius of a circle (Seeber and Sorlien, 2000). From our interpretation of the SJT and hanging wall fold, this solution defines a 4,500 m radius of curvature. The origin of the circle is located in the backlimb of the Tugulu fold, in the vicinity of where we have observed a distinct fanning of terrace fold dips (Figure 4B). However, the origin of the defined circle is ~1,200 m above sea level. The absolute elevations of these terraces south of the backlimb fold limb are ~1,000-1,100 m. Thus, terrace folding would be forced to occur over a very narrow horizontal distance. In this kinematic model, portions of terraces above the planar ramp beyond the region of fault curvature (θ_2), terraces would be rigidly uplifted and would not undergo folding by limb rotation (Seeber and Sorlien, 2000; Amos et al., 2007; Hu et al., 2015). In contrast, we observe Quaternary terraces (T0-T3) folded across the entire extent of the θ_2 fault ramp. We note that the width of the T3 fold limb is ~1.8 km whereas the width of the T4 fold limb is ~900 m. Thus, in this interpretation, the T3 terrace would have experienced significantly more slip than T4 equating to ~1-2 orders of magnitude more fault slip than suggested by the structural relief (Table 3). Based on this analysis, we conclude that a listric fault-bend fold kinematic model (Seeber and Sorlien, 2000; Amos et al., 2007; Hu et al., 2015) is not consistent our integrated surface and subsurface data constraints. We note that in the absence of our subsurface data, the listric fault-bend fold model may be permissible because we would not have independent constraints on the width of the fault curvature (e.g. Amos et al., 2007; Hu et al., 2015). However, as we show with our mechanical model, fault-bend folding is consistent with both the surface and subsurface data constraints for this thrust sheet. This highlights the importance of subsurface data constraints to develop accurate kinematic models of fold growth; the occurrence of progressive limb rotation in growth strata or terrace folds may be consistent with a fault-bend fold solution (e.g. Dolan et al., 2003; Benesh et al., 2007; Leon et al., 2007; 2009).

Appendix B: Terrace Profile Extraction Procedure

Terrace Mapping

We mapped terraces across the Tugulu anticline along the Taxi He valley using the 1-m digital elevation model data set. For the young river terraces along the active stream channel, we mapped the top of terrace treads by extracting linear profiles along several transects of terrace segments. Only the T4 terrace was fully continuous across one side of the Taxi He (Figure 3), requiring the T5 and T6 terraces to involve profiles from both sides of the river valley. We assumed that a terrace tread directly across a river valley (perpendicular to the flow direction) within <70cm change in elevation was considered a terrace of equal age. We found the terraces interpreted for T5 and T6 had elevation changes that were negligible when compared to the natural variability of these terrace elevations (~35 cm). Interpretations of discontinuous Quaternary terraces (Figure 4C) required mapping of a loess cap contact with the fluvial deposits beneath, marking the top of the terrace tread. These features were readily identifiable in the field and DEM, facilitating relatively straightforward mapping procedures. However, given their discontinuous state, these features required iterative quality control both internally when mapping with the topographic data, as well as confirmation in the field. This procedure included comparison of terrace elevation, dip, lithology wherever two terrace remnants were discontinuous. This was particularly important in places where we were required to jump correlate terraces across the Taxi or Tugulu He (Figure 3C).

Correcting for Depositional Gradient

In order to quantify tectonic deformation, the original depositional gradient should be estimated to properly assess uplift and fold dips. This procedure can be difficult without some constraint on the undeformed geometry of a terrace (e.g. Finnegan, 2013). The continuity of terraces in southern Junggar allow us to make reasonable assumptions on their depositional gradients. The raw terrace profiles for T4-T6 terraces to the south of any axial surfaces likely represent their depositional gradient as there are no known structures that would have warped or folded these terraces immediately south of Tugulu (Figure 3C). Each of these terraces parallel the present-day Taxi He channel where they overlie the underlying detachment dip domain, indicating the Taxi He has maintained a relatively constant gradient since the deposition of T4 (Figure 6A). We remove this regional dip of 1.1° to reorient terrace elevations relative to the Taxi He. In this reference frame (Figure 6B), any significant deviations from negligible dip may indicate structural relief due to fault slip on the SJT. The T0-T3 terraces are farther removed from the present-day Taxi He channel and mimic a paleo-trajectory significantly different than the Holocene Taxi He meandering (Figure 3C). The azimuths of these terraces more closely resemble a presently dry streambed that is adjacent to these terraces – which we refer to as the Tugulu He –, west of the Taxi He (Figure 3C). T0 and T1 are not preserved outside of the Tugulu fold limb, whereas T2 and T3 can be mapped south of the fold over a distance that sufficiently constrains their original depositional gradients (Figure 3C). The T2 and T3 terraces have an undeformed dip of 1.3° above the underlying detachment, parallel to the gradient of the Tugulu He (Figure 6A). Given the apparently long-term steady river gradients from the Taxi and Tugulu systems, we assume T1 and

T0 had the same 1.3° depositional gradient. We remove this gradient and produce residual terrace profiles relative to the Tugulu He for T0-T3 (Figure 6C). All subsequent structural analysis is conducted using these residual terrace profiles. We document our assessment of uncertainties related to the vertical position of terrace interpretations in Appendix C.

Appendix C: Uncertainties in Slip and Slip Rate Calculations

Fault Slip Uncertainty

We use structural relief measured in fluvial terrace profiles to quantify total fault slip along the SJT since the times of terrace abandonment. We apply a 1.2 m uncertainty for the all of the terrace elevation data associated with variations in the gravel veneer thickness and the resolution limits of the topographic dataset (70 cm). For Quaternary terraces, we add an additional ±1.5m uncertainty due to horizontal measurement error when interpreting terraces to account the potential for steep gradients (~35° in places) at loess-gravel contacts, along which these older terraces were mapped. These uncertainties encompass those related to selecting a single elevation to represent the position of a natural terrace tread (e.g. natural variations). Dip measurements along the SJT fault geometry were estimated to be ~1.5° by considering the range of hanging wall reflector and thrust dip orientations permissible while still producing a viable cross-section across the entire A-A' section that is consistent with fault-bend folding (Suppe, 1983).

Slip Rate Uncertainty

The mean values of the terrace data across the Tugulu anticline indicate a maximum slip rate of ~7.0 mm/yr at ~250 ka that has since decreased to a constant rate of ~1.3 mm/yr throughout the Holocene. We assess our conclusion of a decelerating SJT slip rate with a straightforward f-test simulation that considers terrace age uncertainties as well as fault slip uncertainties. For each simulation, fit two functions to these data: 1st- and 2nd-order polynomials that both run through the origin (e.g. Supplemental Figure 1A). For both functions we evaluate the model residuals:

$$\chi^2 = \sum_i \frac{r_i^2}{\sigma_i^2}$$

where r_i are the slip residuals (e.g. Supplemental Figure 1B) and σ_1 are the 1-sigma slip uncertainties. When χ^2 for the 2nd-order polynomial fit is less than that for the 1st-order polynomial fit to the data, a decelerating slip rate is considered to have passed our f-test. We run 5000 simulations that randomly draw from the terrace age distributions and perform the f-test for each simulation. All 5000 2nd-order polynomial fits pass this f-test. Thus, a decelerating slip rate is a more robust description of our terrace data than a linear slip rate model to describe the same data.

We further evaluate how well the 2nd-order polynomials describe the terrace data relative to linear slip rate models by evaluating the modified Akaike Information Criterion (AICc):

$$AICc = 2k - 2\ln L + \frac{2k(k+1)}{n-k-1}$$

where k is the number of parameters in the model, L is the maximum of the likelihood function for the studied model and n is the sample size. AIC can be used to evaluate the amount of information lost by a describing a dataset. The modified form used here (AICc) incorporates a penalty to avoid over-fitting to small datasets. The 2nd-order polynomial functions systematically reduce the amount of lost information (lower AICc) relative to the constant slip rate functions (Supplemental Figure 2). This indicates that the decreasing slip rate models described by the 2nd-order polynomial functions to our terrace data and uncertainties are consistently a better fit than a linear function to the same data.

ACKNOWLEDGMENTS

This work was partially funded by the Harvard China Fund, National Natural Science Foundation of China (grants 41172183 and 41472176) and PetroChina. Taylor Perron provided important insight into procedures for identifying fluvial terraces. Brendan Meade provided helpful discussions related to terrace depositional gradients and statistical hypothesis testing. Yanpeng Sun, Will Thompson-Butler, Yiquan Li and her students provided assistance in the field.

REFERENCES

Adamiec, G., Aitken, M., 1998. Dose-rate conversion factors: update. Ancient TL, v. 16, pp. 37-50.

Amos, C. B., Burbank, D.W., Nobes, D. C., and Read, S.A.L., 2007, Geomorphic constraints on listric faulting: implications for active deformation in the Mackenzie Basin, South Island, New Zealand: Journal of Geophysical Research, v. 112, B03S11, 24 pp.

Arnold, L.J., Roberts, R.G., 2009, Stochastic modelling of multi-grain equivalent dose (D_e) distributions: Implications for OSL dating of sediment mixtures: Quaternary Geochronology, v. 4, pp. 204-230.

Avouac, J.P., Tapponnier, P., Bai, M., You, H., Wang, G., 1993, Active thrusting and folding along the northern Tien Shan and late Cenozoic rotation of the Tarim relative to Dzungaria and Kazakhstan: Journal of Geophysical Research, v. 98, no. B4, p. 6755-6804.

Benesh, N.P., 2010. The mechanics of fault-bend folding and tear-fault systems in the Niger Delta: PhD Dissertation, Harvard University, 124 pp.

Benesh, N.P., Plesch, A., Shaw, J.H. and Frost, E.K., 2007, Investigation of growth fault bend folding using discrete element modeling: Implications for signatures of active folding above blind thrust faults: Journal of Geophysical Research: Solid Earth, v. 112(B3).

Bøtter-Jensen, L., C. E. Andersen, G. A. T. Duller, A. S. and Murray, 2003, Developments in radiation, stimulation and observation facilities in luminescence measurements: Radiation Measurements, v. 37, p. 535-541.

Brandenburg, J.P., 2013. Trishear for curved faults. Journal of Structural Geology, v. 53, p. 80-94.

Brown, N.D., Rhodes, E.J., Antinao, J.L. and McDonald, E.V., 2015. Single-grain post-IR IRSL signals of K-feldspars from alluvial fan deposits in Baja California Sur, Mexico. Quaternary International, 362, pp.132-138.

Burchfiel, B.C., Brown, E.T., Deng, Q., Feng, X., Li, J., Molnar, P., Shi, J., Wu, Z., You, H., 1999, Crustal shortening on the margins of the Tien Shan, Xinjiang, China: International Geology Review, v. 41, no. 8, p. 665-700.

Buylaert, J.P., Murray, A.S., Thomsen, K.J., Jain, M., 2009. Testing the potential of an elevated temperature IRSL signal from K-feldspar. Radiation Measurements 44, 560-565.

Charreau, J., J-P. Avouac, Y. Chen, S. Dominguez and S. Gilder (2008), Miocene to present kinematics of fault-bend folding across the Huerguosi anticline, northern Tianshan (China), derived from structural, seismic, and magnetostratigraphic data, Geology, 36, p. 871-874.

Chen, Y.-G., Lai, K.-Y., Lee, Y.-H., Suppe, J., Chen, W.-S., Lin, Y.-N. N., Wang, Y., Hung, J.-H., Kuo, Y.-T., 2007, Coseismic fold scarps and their kinematic behavior in the 1999 Chi-Chi earthquake Taiwan: Journal of Geophysical Research, vol. 112, B03S02, 15 pp.

Cook, K.L., Turowski, J.M. and Hovius, N., 2014, River gorge eradication by downstream sweep erosion: Nature Geoscience, 7(9), pp.682-686.

Cristallini, E.O. and Allmendinger, R.W., 2002. Backlimb trishear: a kinematic model for curved folds developed over angular fault bends. Journal of Structural Geology, 24(2), pp.289-295.

Cundall, P.A. and Strack, O.D., 1979. A discrete numerical model for granular assemblies. Geotechnique, 29(1), pp.47-65.

Dahlstrom, C.D., 1970, Structural geology in the eastern margin of the Canadian Rocky Mountains: Bulletin of Canadian Petroleum Geology, v. 18(3), pp.332-406.

Dolan, J.F., Christofferson, S., Shaw, J.H.,2003, Recognition of paleoearthquakes on the Puente Hills blind thrust fault, Los Angeles, California: Science, v. 300, p. 115-118.

Erslev, E.A., 1991, Trishear fault propagation folding: Geology, v. 19, p. 617-620.

Finnegan, N. J., 2013, Interpretation and downstream correlation of bedrock river terrace treads created from propagating knickpoints: Journal of Geophysical Research: Earth Surface, v. 118(1), p.54-64.

Galbraith, R.F., Roberts, R.G., Laslett, G.M., Yoshida, H. and Olley, J.M., 1999. Optical dating of single and multiple grains of quartz from jinmium rock shelter, northern australia: part i, experimental design and statistical models*. Archaeometry, 41(2), pp.339-364.

Gold, R.D., Cowgill, E., Wang, X.F. and Chen, X.H., 2006. Application of trishear fault-propagation folding to active reverse faults: examples from the Dalong Fault, Gansu Province, NW China. Journal of Structural Geology, 28(2), pp.200-219.

Gong, Z., Li, S. H., & Li, B., 2014, The evolution of a terrace sequence along the Manas River in the northern foreland basin of Tian Shan, China, as inferred from optical dating: Geomorphology, v. 213, p. 201-212.

Guan, S., Stockmeyer, J. M., Shaw, J.H., Plesch, A. and Zhang, J., 2016, Structural inversion, imbricate wedging, and out-of-sequence thrusting in the southern Junggar fold-and-thrust belt, northern Tian Shan, China: AAPG Bulletin, in press, DOI:10.1306/04041615023.

Hardy, S. and C. D. Connors, 2006, Short note: a velocity description of shear fault-bend folding: Journal of Structural Geology, v. 28, no. 3, p. 536-543.

Hardy, S. and Poblet, J., 1994, Geometric and numerical model of progressive limb rotation in detachment folds: Geology, v. 22(4), p. 371-374.

Hu, X., B. Pan, E. Kirby, H. Gao, Z. Hu, B. Cao, H. Geng, Q. Li, and G. Zhang, 2015, Rates and kinematics of active shortening along the eastern Qilian Shan, China, inferred from deformed fluvial terraces: Tectonics, v. 34(12), p. 2478–2493

Hubert-Ferrari, A., Suppe, J., Gonzalez-Mieres, R., Wang, X., 2007, Mechanisms of active folding of the landscape (southern Tian Shan, China): Journal of Geophysical Research, v. 112, B03S09, 39 pp.

Hughes, A.N. and Shaw, J.H., 2014, Fault displacement-distance relationships as indicators of contractional fault-related folding style: AAPG bulletin, v. 98(2), p.227-251.

Hughes, A.N. and Shaw, J.H., 2015. Insights into the mechanics of fault-propagation folding styles. Geological Society of America Bulletin, 127(11-12), pp.1752-1765.

Hughes, A.N., Benesh, N.P. and Shaw, J.H., 2014. Factors that control the development of fault-bend versus fault-propagation folds: Insights from mechanical models based on the discrete element method (DEM). Journal of Structural Geology, 68, pp.121-141.

Huntley, D.J., Baril, M., 1997. The K content of the K-feldspar being measured in optical dating or in thermoluminescence dating. Ancient TL, v. 15, pp. 11-13.

Huntley, D.J., Lamothe, M., 2001. Ubiquity of anomalous fading in K-feldspars and the measurement and correction for it in optical dating. Canadian Journal of Earth Science, 38, pp. 1093-1106.

Ishiyama, T., Mueller, K., Sato, H., & Togo, M. (2007). Coseismic fault-related fold model, growth structure, and the historic multisegment blind thrust earthquake on the basement-involved Yoro thrust, central Japan. J. Geophys. Res., 112(B3), 22 pp.

Johnson, K.N. and Finnegan, N.J., 2015. A lithologic control on active meandering in bedrock channels. Geological Society of America Bulletin, 127(11-12), pp.1766-1776.

Lavé, J., and Avouac, J.P., 2000, Active folding of fluvial terraces across the Siwaliks Hills, Himalayas of central Nepal: Journal of Geophysical Research, v. 105, no. B3, p. 5735-5770.

Le Béon, M., Suppe, J., Jaiswal, M.K., Chen, Y.G. and Ustaszewski, M.E., 2014. Deciphering cumulative fault slip vectors from fold scarps: Relationships between long-term and coseismic deformations in central Western Taiwan. Journal of Geophysical Research: Solid Earth, 119(7), pp.5943-5978.

Leon, L.A., Christofferson, S.A., Dolan, J.F., Shaw, J.H. and Pratt, T.L., 2007, Earthquake-by-earthquake fold growth above the Puente Hills blind thrust fault, Los Angeles, California: implications for fold kinematics and seismic hazard: Journal of Geophysical Research: Solid Earth, v. 112(B3).

Leon, L.A., Dolan, J.F., Shaw, J.H. and Pratt, T.L., 2009, Evidence for large Holocene earthquakes on the Compton thrust fault, Los Angeles, California: Journal of Geophysical Research: Solid Earth, 114(B12).

Leonard, M. (2010), Earthquake fault scaling: self-consistent relating of rupture length, width, average displacement, and moment release, Bull. Seismol. Soc. Am., 100, 1971-1988, doi:10.1785/0120090189.

Lu, H., Burbank, D. W., Li, Y., & Liu, Y. (2010). Late Cenozoic structural and stratigraphic evolution of the northern Chinese Tian Shan foreland. Basin Research, 22(3), 249-269.

Medwedeff, D. A., 1989, Growth fault-bend folding at southeast Lost Hills, San Joaquin Valley, California: AAPG Bulletin, v. 73(1), p. 54-67.

Medwedeff, D.A. and Suppe, J., 1997. Multibend fault-bend folding. Journal of Structural Geology, 19(3), pp.279-292.

Molnar, P., Brown, E.T., Burchfiel, B.C., Deng, Q., Feng, X., Li, J., Raisbeck, G.M., Shi, J., Wu, Z., Yiou, F., You, H., 1994, Quaternary Climate Change and the Formation of River Terraces across Growing Anticlines on the North Flank of the Tien Shan, China: The Journal of Geology, v. 102, p. 583-602.

Molnar, P. and Ghose, S., 2000. Seismic moments of major earthquakes and the rate of shortening across the Tien Shan. Geophysical Research Letters, 27(16), pp.2377-2380.

Morgan, J.K., 1999. Numerical simulations of granular shear zones using the distinct element method: 2. Effects of particle size distribution and interparticle friction on mechanical behavior. Journal of Geophysical Research: Solid Earth, 104(B2), pp.2721-2732.

Morgan, J.K., 2015. Effects of cohesion on the structural and mechanical evolution of fold and thrust belts and contractional wedges: Discrete element simulations. Journal of Geophysical Research: Solid Earth, 120(5), pp.3870-3896.

Mueller, K., J. Champion, M. Guccione, and K. Kelson, , 1999, Fault slip rates in the modern New Madrid seismic zone. Science, v. 286(5442), p.1135-1138.

Murray, A.S. and Wintle, A.G., 2000, Luminescence dating of quartz using an improved single-aliquot regenerative-dose protocol: Radiation Measurements, v. 32, p. 57-73.

Nelson, M.R., McCaffrey, R., Molnar, P., 1987, Source parameters for 11 earthquakes in the Tien Shan, Central Asia, determined by P and SH waveform inversion: Journal of Geophysical Research, v. 92, no. B12, p. 12629-12648.

Poisson, B., 2002. Impact du climat et de la tectonique sur l'évolution géomorphologique d'un piémont-Exemple du piémont Nord du Tian Shan depuis la fin du Pléistocène (Doctoral dissertation, Université Paris Sud-Paris XI).

Poisson, B. and Avouac, J.P., 2004, Holocene hydrological changes inferred from alluvial stream entrenchment in north Tian Shan (Northwestern China): The Journal of Geology, v. 112, p. 231-249.

Pratt, T. L., Shaw, J. H., Dolan, J. F., Christofferson, S., Williams, R. A., Odum, J. K., Plesch, A., 2002, Shallow folding imaged above the Puente Hills blind-thrust fault, Los Angeles, California: Geophysical Research Letters, v. 29, p. 18-1 to 18-4.

Prescott, J., Hutton, J., 1994. Cosmic ray contributions to dose rates for luminescence and ESR dating: large depths and long-term time variations. Radiation Measurements, v. 23, pp. 497-500.

Rhodes, E.J., 2015. Dating sediments using potassium feldspar single-grain IRSL: Initial methodological considerations. Quaternary International, 362, pp.14-22.

Rich, J.L., 1934, Mechanics of low-angle overthrust faulting as illustrated by Cumberland thrust block, Virginia, Kentucky, and Tennessee: AAPG Bulletin, v. 18(12), pp.1584-1596.

Scharer, K.M., Burbank, D.W., Chen, J., Weldon, R.J., 2006, Kinematic models of fluvial terraces over active detachment folds: constraints on the growth mechanisms of the Kashi-Atushi fold system, Chinese Tian Shan: Geological Society of America Bulletin, v. 118, no. 7-8, p. 1006-1021.

Seeber, L. and Sorlien, C.C., 2000. Listric thrusts in the western Transverse Ranges, California. Geological Society of America Bulletin, 112(7), pp.1067-1079.

Shaw, J.H., Connors, C., Suppe, J., eds., 2005, Seismic interpretation of contractional fault-related folds: An AAPG seismic atlas, AAPG Studies in Geology 53, 156 pp.

Shaw, J.H., F. Bilotti, and P. Brennan, 1999, Patterns of imbricate thrusting: Geological Society of America Bulletin, v. 111, p. 1140-1154.

Shaw, J.H. and J. Suppe, 1994, Active faulting and growth folding in the eastern Santa Barbara channel, California: Geological Society of America Bulletin, v. 100, no. 5, p. 607-626.

Shaw, J.H. and J. Suppe, 1996, Earthquake hazards of active blind-thrust faults under the central Los Angeles basin, California: Journal of Geophysical Research: Solid Earth, 101(B4), p. 8623-8642.

Shaw, J.H., Hook, S.C. and Suppe, J., 1994. Structural trend analysis by axial surface mapping. AAPG bulletin, 78(5), pp.700-721.

Shaw, J.H., Plesch, A., Dolan, J.F., Pratt, T., Fiore, P., 2002, Puente Hills blind thrust system, Los Angeles basin, California: Bulletin of the Seismological Society of America, v. 92, p. 2946-2960.

Smedley, R.K., Duller, G.A.T., Roberts, H.M., 2015. Bleaching of the post-IR IRSL signal from individual grains of K-feldspar: Implications for single-grain dating. Radiation Measurements, v. 79, pp. 33-42.

Stein, R.S., and King, G.C.P., 1984, Seismic potential revealed by surface folding: 1983 Coalinga, California, earthquake: Science, v. 224, no. 4651, p. 869-872.

Stockmeyer, J. M., J. H. Shaw, and G. Shuwei, 2014, Seismic hazards of multisegment thrust-fault ruptures: insights from the 1906 Mw 7.4-8.2 Manas, China, Earthquake, Seis. Res. Lett., v. 85, p. 801-808, doi: 10.1785/0220140026.

Strayer, L.M., Erickson, S.G. and Suppe, J., 2004. Influence of growth strata on the evolution of fault-related folds—distinct-element models.

Suppe, J., 1983, Geometry and kinematics of fault-bend folding: American Journal of Science, v. 283, p. 684-721.

Suppe, J. and Medwedeff, D.A., 1990, Geometry and kinematics of fault-propagation folding: Eclogae Geologicae Helvetiae, v. 83, no. 3, p. 409-454.

Suppe, J., C. D. Connors, and Y. Zhang, 2004, Shear fault-bend folding, in: McClay, K.R., ed., Thrust tectonics and hydrocarbon systems: AAPG Memoir 82, p. 303-323.

Suppe, J., F. Sabat, J. Muñoz, J. Poblet, E. Roca, and J. Vergés, 1997, Bed-by-bed fold growth by kink-band migration: Saint Llorenç de Morunys, eastern Pyrenees: Journal of Structural Geology, v. 19, no. 3-4, p. 443-461.

Suppe, J., G. T. Chou, and S. C. Hook, 1992, Rates of folding and faulting determined from growth strata, in K. R. McClay ed., Thrust tectonics: Springer, p. 105- 121.

Thiel, C., Buylaert, J.-P., Murray, A.S., Terhorst, B., Hofer, I., Tsukamoto, S., Frechen, M., 2011. Quaternary International 234, 23-31.

Thompson, C.T., Weldon, R.J., Rubin, C.M., Abdrakhmatov, K., Molnar, P., Berger, G.W., 2002, Late Quaternary slip rates across the central Tien Shan, Kyrgyzstan, central Asia: Journal of Geophysical Research, v. 107, no. B9, p. ETC 7-1–7-32.

Wells, D.L., and K.J. Coppersmith (1994), New empirical relationships among magnitude, rupture length, rupture width, rupture area, and surface displacement, Bull. Seismol. Soc. Am., 94, 974-1002.

Yue, L.F., Suppe, J. and Hung, J.H., 2011, Two contrasting kinematic styles of active folding above thrust ramps, Western Taiwan: in Thrust Fault Related Folding (eds. McClay et al).

TABLES

Table 1. Dosimetry data for individual samples and single-grain post-IR IRSL depositional ages for terraces.

Unit	Field code	% K	Th (ppm)	U (ppm)	Depth (m)	Latitude (°N)	Longitude (°E)	Elevation (m.a.s.l.)	Total dose rate (Gy/ka)	Terrace age (ka)
T8	TGL-T8-OSL10	2.0 ± 0.1	4.9 ± 0.2	1.38 ± 0.07	1.63	44.070	86.341	822	3.411 ± 0.171	
T8	TGL-T8-OSL11	2.0 ± 0.1	4.4 ± 0.2	1.44 ± 0.07	1.98	44.070	86.341	822	3.382 ± 0.171	$4.0\ ^{+3.2}/_{-1.8}$
T8	TGL-T8-OSL12	1.5 ± 0.1	5.9 ± 0.3	1.61 ± 0.08	2.57	44.070	86.341	822	3.033 ± 0.139	
T6	TGL-T6-OSL7	2.2 ± 0.1	4.6 ± 0.2	1.45 ± 0.07	0.30	44.072	86.338	864	3.636 ± 0.190	
T6	TGL-T6-OSL8	2.0 ± 0.1	6.3 ± 0.3	1.80 ± 0.09	0.46	44.072	86.338	864	3.638 ± 0.177	$5.6\ ^{+4.1}/_{-2.4}$
T6	TGL-T6-OSL9	1.9 ± 0.1	4.1 ± 0.2	1.44 ± 0.07	0.73	44.072	86.338	864	3.299 ± 0.164	
T5	TGL-T5-OSL4	2.1 ± 0.1	5.7 ± 0.3	1.96 ± 0.10	0.70	44.072	86.338	872	3.723 ± 0.183	
T5	TGL-T5-OSL5	1.9 ± 0.1	4.3 ± 0.2	1.67 ± 0.08	1.15	44.072	86.338	872	3.355 ± 0.165	$9.4\ ^{+5.1}/_{-3.3}$
T5	TGL-T5-OSL6	2.1 ± 0.1	4.6 ± 0.2	1.59 ± 0.08	1.52	44.072	86.338	872	3.538 ± 0.179	
T4	TGL-T4-OSL1	2.7 ± 0.1	6.1 ± 0.3	1.90 ± 0.10	0.65	44.065	86.335	894	4.312 ± 0.227	
T4	TGL-T4-OSL2	1.9 ± 0.1	4.8 ± 0.2	1.61 ± 0.08	1.30	44.065	86.335	894	3.372 ± 0.165	
T4	TGL-T4-OSL3	2.0 ± 0.1	5.5 ± 0.3	1.70 ± 0.09	2.75	44.065	86.335	894	3.501 ± 0.173	$17.5\ ^{+13.4}/_{-7.6}$
T4	TGL-T4-OSL13	2.0 ± 0.1	3.9 ± 0.2	1.50 ± 0.08	1.25	44.114	86.354	777	3.391 ± 0.170	
T4	TGL-T4-OSL14	1.8 ± 0.1	4.1 ± 0.2	1.51 ± 0.08	1.60	44.114	86.354	777	3.206 ± 0.156	
T3	TGL-T3-OSL15	2.1 ± 0.1	5.9 ± 0.3	2.99 ± 0.15	0.80	44.071	86.328	959	3.956 ± 0.188	
T3	TGL-T3-OSL16	2.1 ± 0.1	8.6 ± 0.4	2.78 ± 0.14	1.60	44.071	86.328	959	3.879 ± 0.180	$46.3\ ^{+23.6}/_{-15.6}$
T3	TGL-T3-OSL17	2.0 ± 0.1	5.4 ± 0.3	1.85 ± 0.09	2.40	44.071	86.328	959	3.529 ± 0.174	
T2	TGL-T2-OSL19	1.5 ± 0.1	4.9 ± 0.2	2.40 ± 0.12	0.80	44.065	86.318	996	3.192 ± 0.143	
T2	TGL-T2-OSL20	2.2 ± 0.1	6.0 ± 0.3	2.35 ± 0.12	1.40	44.065	86.318	996	3.903 ± 0.192	$106.4\ ^{+76.6}/_{-44.5}$
T2	TGL-T2-OSL21	2.1 ± 0.1	5.5 ± 0.3	2.17 ± 0.11	2.05	44.065	86.318	996	3.743 ± 0.184	
T1	TGL-T1-OSL23	2.2 ± 0.1	4.9 ± 0.2	1.71 ± 0.09	0.65	44.067	86.314	1084	3.753 ± 0.190	
T1	TGL-T1-OSL24	2.0 ± 0.1	5.8 ± 0.3	2.21 ± 0.11	1.30	44.067	86.314	1084	3.649 ± 0.176	$182.1\ ^{+39.2}/_{-32.3}$
T1	TGL-T1-OSL25	2.1 ± 0.1	5.7 ± 0.3	2.28 ± 0.11	1.75	44.067	86.314	1084	3.769 ± 0.184	
T0	TGL-T0-OSL15	1.9 ± 0.1	5.2 ± 0.3	1.91 ± 0.10	0.69	44.069	86.309	1102	3.496 ± 0.168	
T0	TGL-T0-OSL16	1.9 ± 0.1	6.4 ± 0.3	2.27 ± 0.11	1.05	44.069	86.309	1102	3.652 ± 0.172	$236.7\ ^{+45.9}/_{-38.5}$
T0	TGL-T0-OSL17	1.7 ± 0.1	5.8 ± 0.3	2.02 ± 0.10	0.77	44.069	86.309	1102	3.370 ± 0.156	

TABLE 2. SJT FAULT SLIP FROM HOLOCENE FAULT SCARPS

	T4	T5	T6
Age (ka)	17.50	9.40	5.60
z_4 (m)	61.80	50.02	35.13
z_{fw} (m)	46.83	41.52	29.72
h_4 (m)	14.97	8.50	5.41
θ_4 (°)	44.50	44.50	44.50
u_4 (m)	**21.4**	**12.1**	**7.7**

TABLE 3. SJT FAULT SLIP FROM QUATERNARY FOLD SCARPS

	T0	T1	T2	T3
Age (ka)	256.7	182.1	106.4	46.3
z_2 (m)	271.30	234.47	104.97	19.19
z_0 (m)	66.04	49.26	26.16	7.44
Δh_2 (m)	205.26	185.21	78.81	11.75
$\sin(\theta_2) - \sin(\theta_0)$	0.40	0.40	0.40	0.40
u_4 (m)	**512.0**	**462.0**	**197.1**	**29.31**

TABLE 4. PHYSICAL PROPERTIES OF THE MECHANICAL FAULT-BEND FOLD

Property	Pre-growth strata	Flexural slip surfaces	Growth strata	Fault surfaces	Boundary wall
Density (kg/m^3)	2500	2500	2500	n/a	n/a
Ball radii (m)†	30-40	22.5-30	22.5-30	n/a	n/a
kn (N/m)	$6.0*10^9$	$6.0*10^9$	$6.0*10^9$	$6.6*10^9$	$6.6*10^9$
ks (N/m)	$6.0*10^9$	$6.0*10^9$	$6.0*10^9$	n/a	n/a
μ§	0.30	0.00	0.30	0.10	0.45
E (GPa)	3.0	3.0	3.0	3.3	3.3
σ_c (MPa)#	10	0	10	n/a	n/a
τ_c (MPa)#	600	0	600	n/a	n/a
Layer thickness (m)	500	125	~250	n/a	n/a

†Randomly generated from a uniform distribution bounded by prescribed range.
§Contact friction.
#Contact bond strength; selected from a Gaussian distribution with a prescribed mean.

FIGURE CAPTIONS

Figure 1: Fault-related fold models and their corresponding distance-displacement plots (Hughes and Shaw, 2014), including measures of surface slip (SS) and fault slip at depth (SD). A) Fault-bend folds (Suppe, 1983) predict constant fault slip up a thrust ramp. The absence of folding through this zone reflects the constant slip at depth along the thrust ramp. B) Simple shear fault-bend folds (Suppe et al., 2004) produce a wide, gentle fold limb above the pre-growth shear interval, where slip increases linearly up the thrust ramp. Note the lack of a fold limb outside of the shear interval, near the structural crest, where slip is constant. C) Fault propagation folds consume fault slip during fault tip propagation. The resultant slip gradient decreases linearly up a thrust ramp. In this latter case, SS can drastically underestimate SD. See text for details. Figure is modified from Hughes and Shaw (2014).

Figure 2: Kinematic models of terrace deformation. A) Classic fault-bend folding (Suppe, 1983) localizes folding across fault bends. Terrace folds develop by kink-band migration. B) Curved hinge fault-bend folds (Suppe et al., 1997) produce fold scarps due to differential uplift that is localized through the curved fault bend. Terrace folds grow by kink-band migration. C) Simple shear fault bend folds (Suppe et al., 2004) produce two dip panels of different magnitudes. More intense folding occurs across the fault bend by kink-band migration. Outboard of this zone across the pre-growth shear interval, more distributed folding occurs by limb rotation. D) Simple shear curved hinge fault-bend folds (Suppe et al., 2004) produce folds of similar styles as described in C but differ only due to kink-band migration across a curved fault zone of finite width, as described in B. E) Listric fault-related folds (Seeber and Sorlien, 2000; Amos et al., 2007) exhibit distributed

folding by limb rotation across a listric fault ramp. In E, the region undergoing limb rotation is localized to the listric fault segment. See text for details.

Figure 3: A) Western China and major tectonic provinces. Black box outlines the southern Junggar basin. Imagery from Google Earth. B) False-color Landsat imagery of the southern Junggar basin study area. Imagery is displayed with bands 7-5-1 (R-G-B). C) Geologic map of surface geology and mapped terraces along the Taxi He valley, across the Tugulu anticline, mapped in the digital elevation model. Section A-A' is shown in Figure 5.

Figure 4: Field observations of fluvial terraces. A) Terraces are preserved across the entire extent of the Taxi He. B) A prominent fault scarp marks the surface-emergent SJT along the entire forelimb of each structure in southern Junggar (Avouac et al., 1993). This provides a record of surface faulting deformation. C) Older, discontinuous terraces in the backlimb of Tugulu provide the ability to quantify surface folding deformation from terrace geometries. Here, terrace treads are marked by the contact between the fluvial deposits below and loess cap above.

Figure 5: Structural interpretation of the SJT fault geometry and hanging wall fold structure across section A-A'. The geometry of the interpreted fault and hanging wall folds are consistent with a fault-bend fold (Suppe, 1983). Projecting axial surfaces (green dashes) to the Earth's surface provide a straightforward method for relating surface deformation observations to subsurface structure (e.g. Shaw et al., 1994). See text for details. Satellite imagery and digital elevation model are displayed at 3:1 vertical exaggeration. Seismic data is displayed at 1:1.

Figure 6: A) Raw terrace profiles used for structural analysis. T0 is the oldest mapped terrace; T6 is the youngest. B) Residual profiles of the Holocene terraces (T4-T6) exhibit abrupt uplift and folding across several active axial surfaces implied by our structural interpretation (Figure 5). Little to no folding is apparent between fault bends. This structural relief is restored across the fault scarp. C) Residual profiles of the Quaternary terraces (T0-T3) are preserved across the southern-most SJT synclinal fault bends. However, they record tens to hundreds of meters of structural relief, developed by surface folding. See text for details. See Appendix B for details on terrace mapping and removing depositional gradients.

Figure 7: Terrace geochronology across the Taxi He valley. A Bayesian model assuming stratigraphic consistency of terraces is used to produce the posterior age distributions. See text for details.

Figure 8: Schematic diagram illustrating the different measures of fold scarp relief used to estimate fault slip since the time of terrace abandonment.

Figure 9: A) Fault slip estimates from Holocene terrace fold scarps across the Tugulu structure from (3). The slope of the best-fit linear regression line yields an estimate of total fault slip experienced by that terrace. The goodness of fit of each regression to the terrace folding data implies a single magnitude of fault slip readily explains all of the fold scarp deformation. B) Estimates of Holocene fault slip and slip rates from terrace faulting and terrace folding are indistinguishable. See text for details.

Figure 10: Mechanical model of a fault-bend fold (Benesh et al., 2007; Benesh, 2010). A) Set-up of the model geometry. Note the change in fault dip is consistent with the dip change across the southern most fault bends of the SJT. Model parameters are summarized in Table 4. B) Final result of the mechanical model after 3000 m of fault slip. Noteworthy observations include 1) pre-growth strata that parallel the fault ramp, consistent with kinematic prediction; 2) an upward narrowing growth fold triangle, which indicates folding by kink-band migration, consistent with the kinematic predictions; 3) uplift and folding is consistently initiated before reaching the fault bend, which is not predicted by the kinematic theory; and 4) a fanning of limb dips, indicating folding by limb rotation, which is not predicted by classic fault-bend folding theories.

Figure 11: A) Dip-slip relations for growth and pre-growth strata in the DEM model. The form of this relation is generalized as a 2^{nd}-order polynomial function that goes through the origin. The constants of the functional form are sensitive to mechanical stratigraphy, grain size, thickness, and other natural heterogeneities. B) Estimates of fault slip versus the observed fault-dip for T1-T4 and the pre-growth constraint for the critical slip required to develop the maximum hanging wall fold dip (Guan et al., 2016; their Figure 4). The slip for T0 can be estimated directly from this functional form. See text for discussion. Fault slip magnitudes for T1-T4 are from Tables 2 and 3.

Figure 12: Slip rate history for the SJT from 250 ka to present. SJT slip rate has decelerated considerably from the Late Quaternary (~7.0 mm/yr) to Holocene (~1.3 mm/yr). See text for details.

Fig. 1

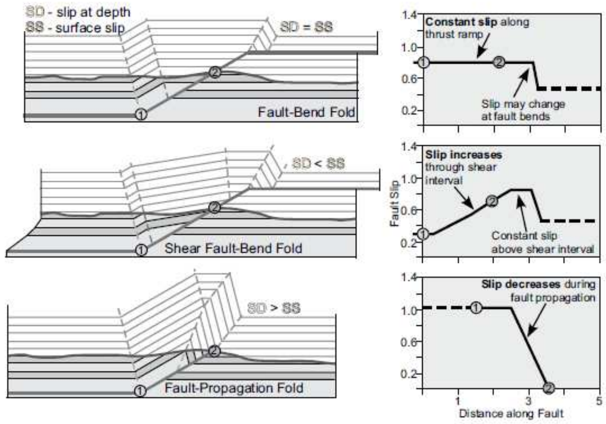

Fig. 2

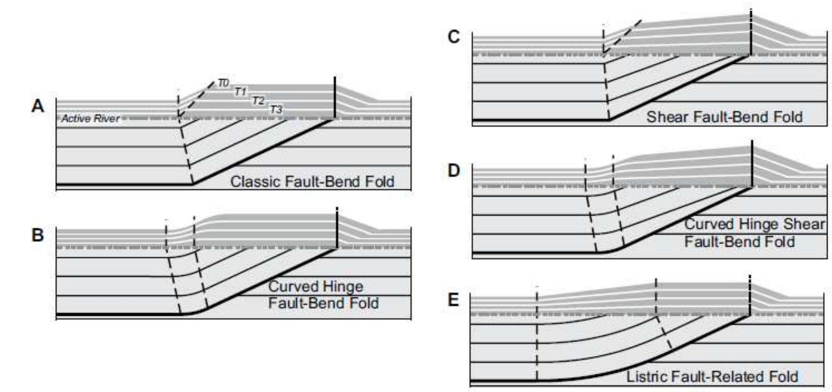

Fig. 3

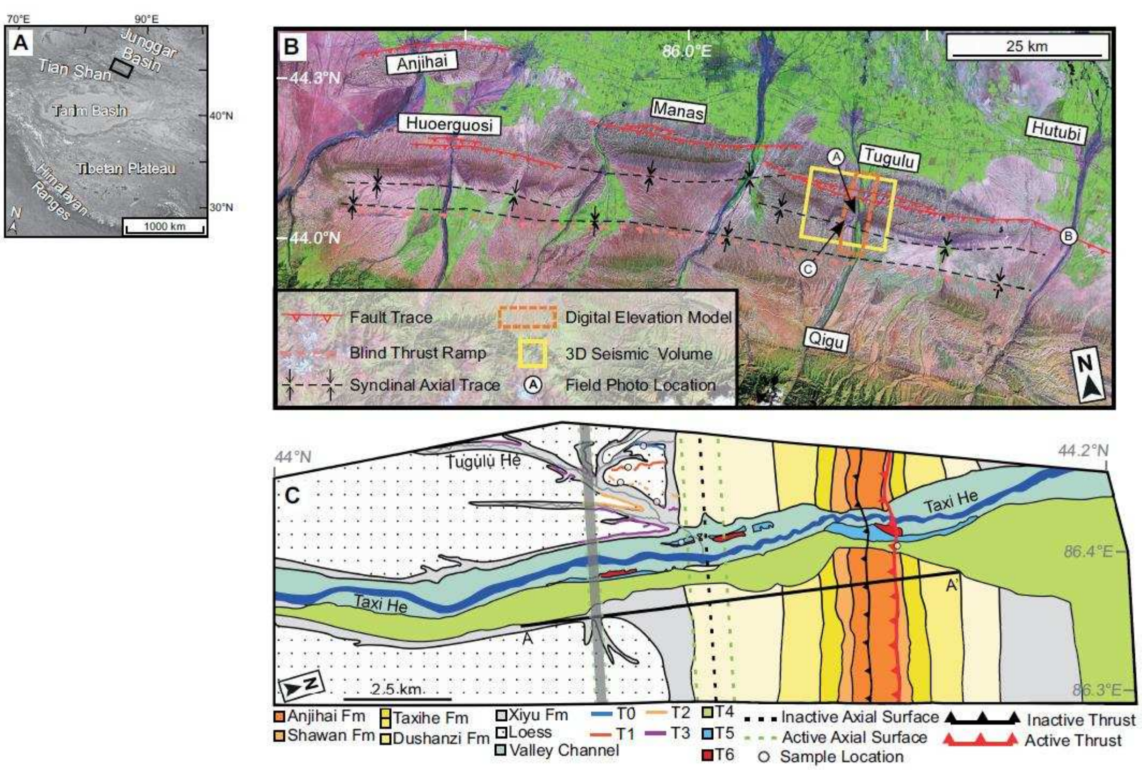

Fig. 4

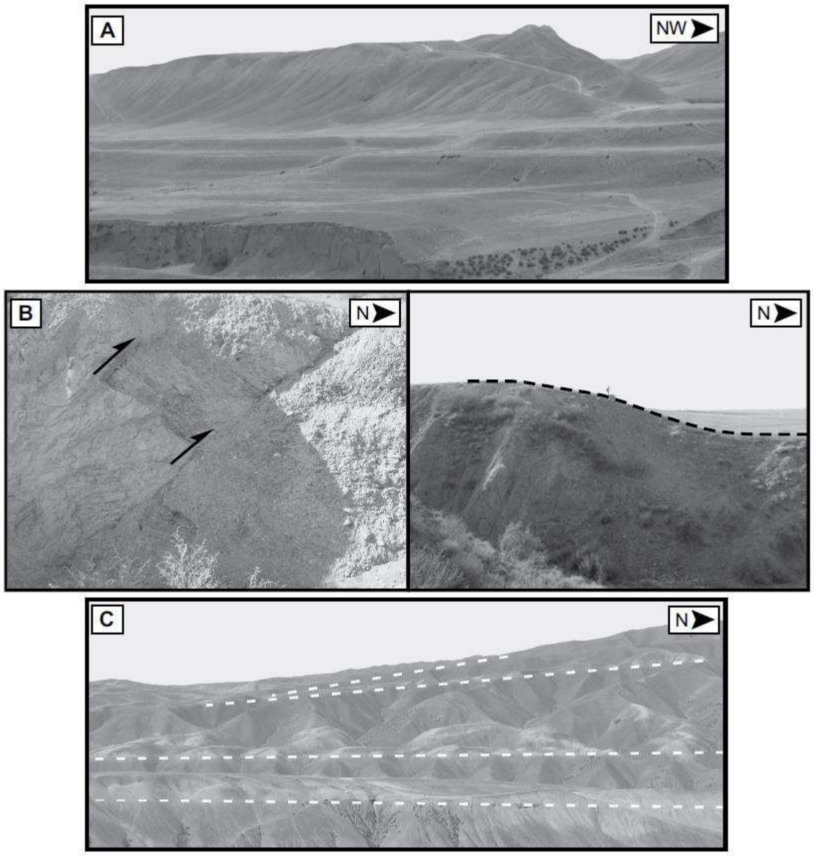
A
NW
B
N
N
C
N

Fig. 5

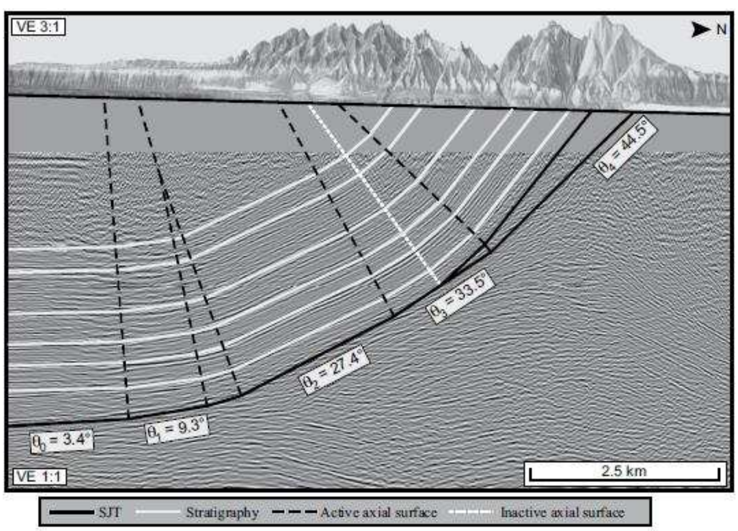
VE 3:1
N
θ_4 = 44.5°
θ_3 = 33.5°
θ_2 = 27.4°
θ_1 = 9.3°
θ_0 = 3.4°
VE 1:1
2.5 km
SJT
Stratigraphy
Active axial surface
Inactive axial surface

Fig. 6

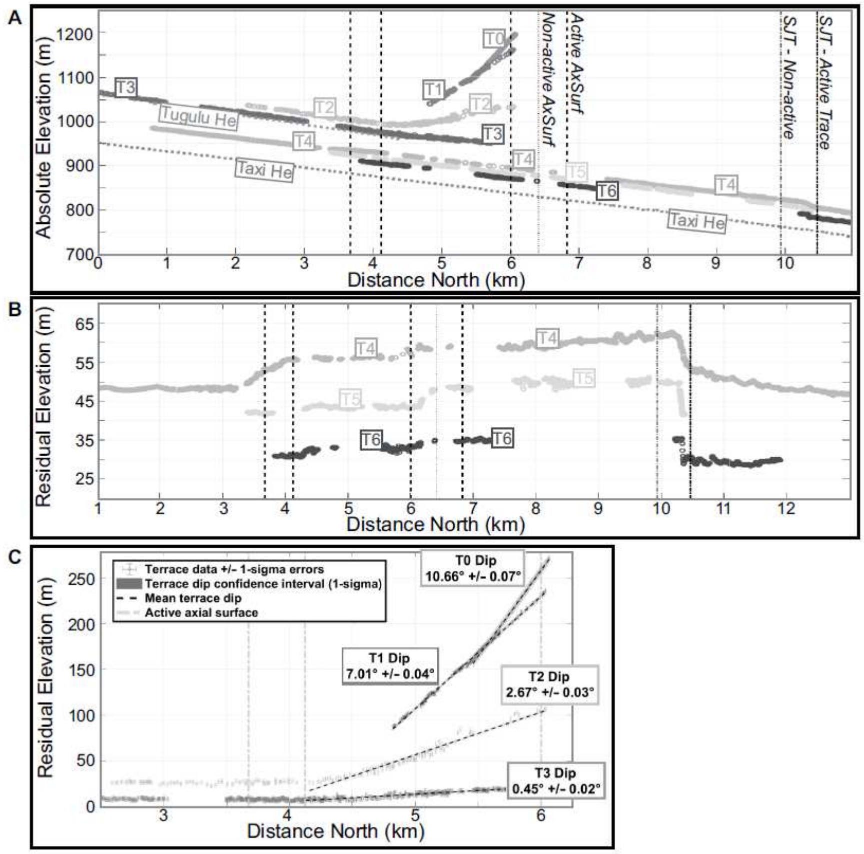

Fig. 7

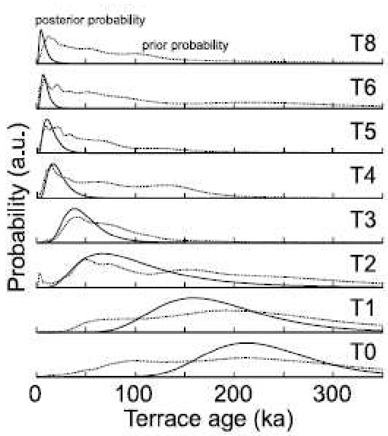

Fig. 8

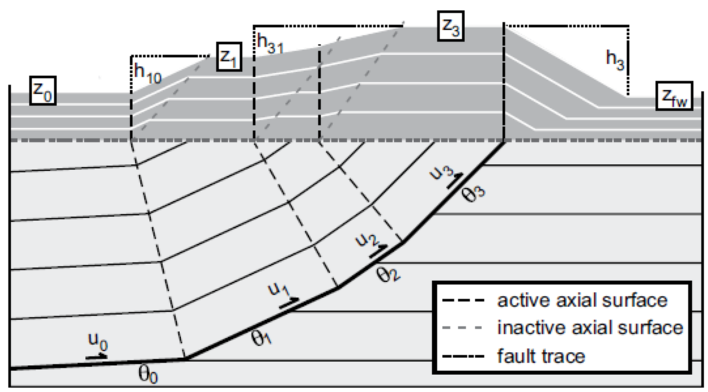

Fig. 9

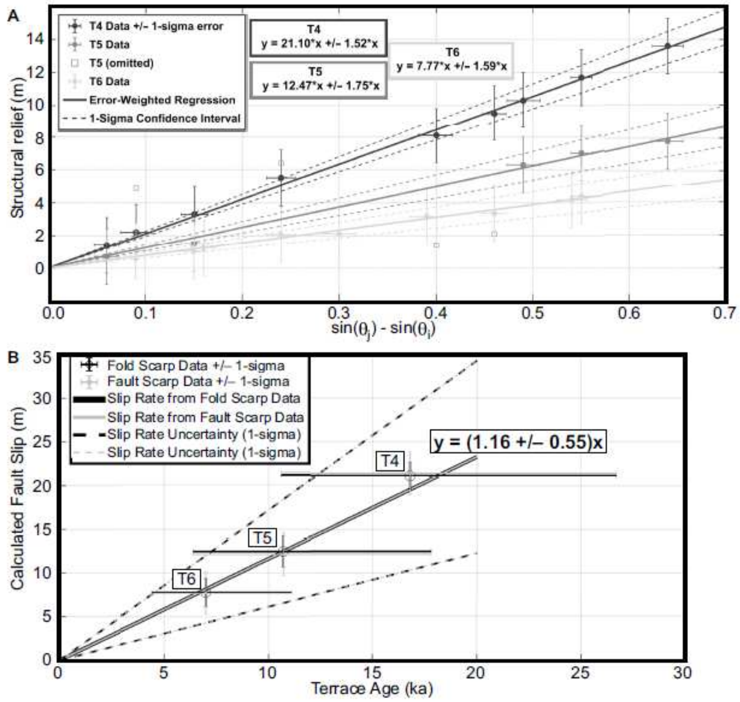
A
T4 Data +/- 1-sigma error
T5 Data
T5 (omitted)
T6 Data
Error-Weighted Regression
1-Sigma Confidence Interval
T4
y = 21.10*x +/- 1.52*x
T5
y = 12.47*x +/- 1.75*x
T6
y = 7.77*x +/- 1.59*x
Structural relief (m)
sin(θj) - sin(θi)
B
Fold Scarp Data +/– 1-sigma
Fault Scarp Data +/– 1-sigma
Slip Rate from Fold Scarp Data
Slip Rate from Fault Scarp Data
Slip Rate Uncertainty (1-sigma)
Slip Rate Uncertainty (1-sigma)
y = (1.16 +/– 0.55)x
T4
T5
T6
Calculated Fault Slip (m)
Terrace Age (ka)

Fig. 10

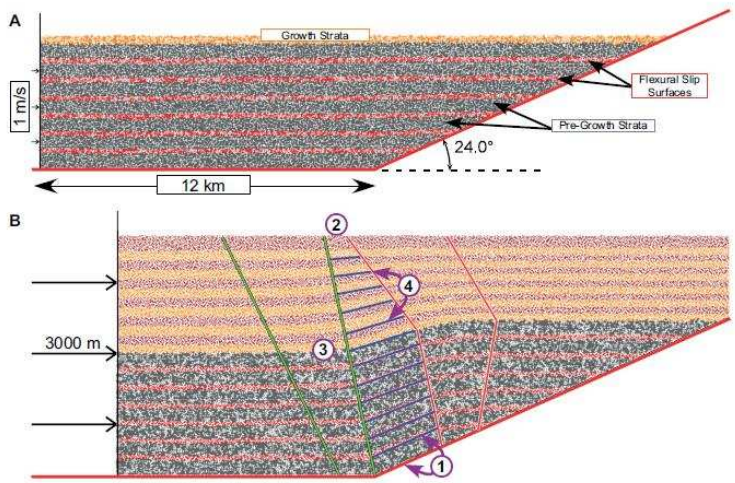
A
Growth Strata
Flexural Slip Surfaces
Pre-Growth Strata
1 m/s
24.0°
12 km
B
3000 m
1
2
3
4

Fig. 11

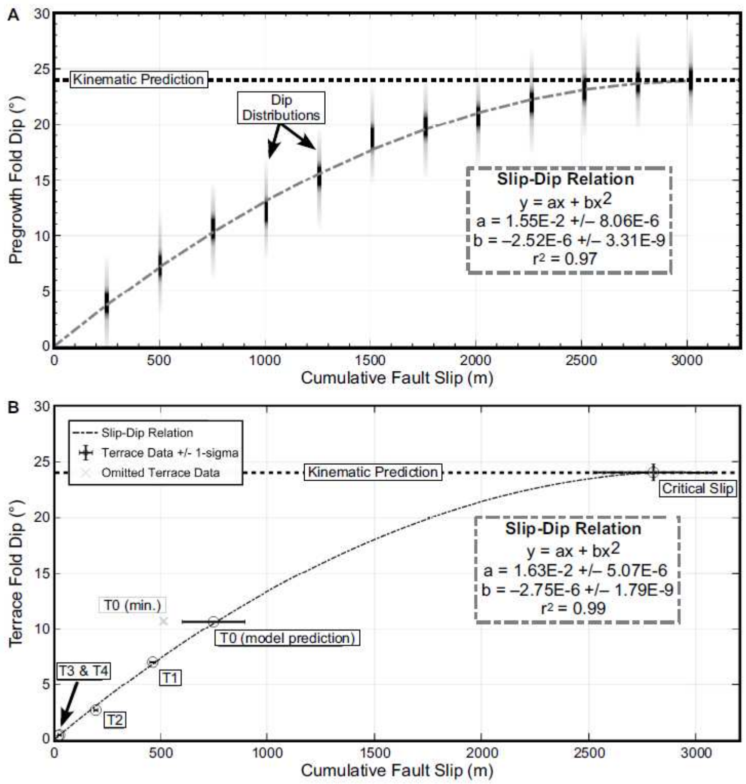

A
Kinematic Prediction
Dip Distributions
Slip-Dip Relation
y = ax + bx2
a = 1.55E-2 +/– 8.06E-6
b = –2.52E-6 +/– 3.31E-9
r2 = 0.97
Pregrowth Fold Dip (°)
Cumulative Fault Slip (m)
B
Slip-Dip Relation
Terrace Data +/- 1-sigma
Omitted Terrace Data
Kinematic Prediction
Critical Slip
Slip-Dip Relation
y = ax + bx2
a = 1.63E-2 +/– 5.07E-6
b = –2.75E-6 +/– 1.79E-9
r2 = 0.99
T0 (min.)
T0 (model prediction)
T3 & T4
T1
T2
Terrace Fold Dip (°)
Cumulative Fault Slip (m)

Fig. 12

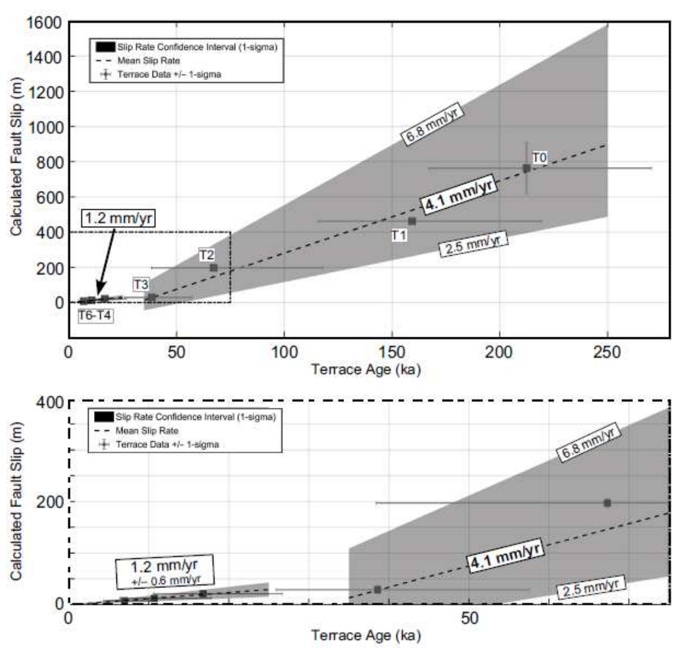

Slip Rate Confidence Interval (1-sigma)
Mean Slip Rate
Terrace Data +/- 1-sigma
6.8 mm/yr
4.1 mm/yr
2.5 mm/yr
1.2 mm/yr
T0
T1
T2
T3
T6-T4
Calculated Fault Slip (m)
Terrace Age (ka)
1.2 mm/yr
+/- 0.6 mm/yr